REPORT NO.
UCB/SEMM-94/18

STRUCTURAL ENGINEERING
MECHANICS AND MATERIALS

ANISOTROPIC MODELING AND NUMERICAL SIMULATION OF BRITTLE DAMAGE IN CONCRETE

BY

Sanjay Govindjee
Gregory J. Kay
and
Juan C. Simo

NOVEMBER 1994

DEPARTMENT OF CIVIL ENGINEERING
UNIVERSITY OF CALIFORNIA
BERKELEY, CALIFORNIA

Anisotropic Modeling and Numerical Simulation of Brittle Damage in Concrete

SANJAY GOVINDJEE

Department of Civil Engineering
Univerisity of California
Berkeley, CA 94720.

GREGORY J. KAY

University of California
Lawrence Livermore National Laboratory
P.O. Box 808
Livermore, CA 94550.

&

JUAN C. SIMO

Division of Applied Mechanics
Department of Mechanical Engineering
Stanford University, Stanford, CA 94305.

§ Abstract

A framework for damage mechanics of brittle solids is exploited in the design and numerical implementation of an anisotropic model for the tensile failure of concrete. The key feature exploited in the analysis is the hypothesis of maximum dissipation, which specifies a unique damage rule for the elastic moduli of the solid once a failure surface is specified. A complete algorithmic treatment of the resulting model is given which renders a useful tool for large scale inelastic finite element calculations. A rather simple three-surface failure model for concrete, containing essentially no adjustable parameters, is shown to produce results in remarkably good agreement with sample experimental data.

§1. Introduction

Degradation of the stiffness properties under loading, an effect commonly referred to as damage, is a complex phenomenon displayed by many materials for which only a limited knowledge of the actual micro-mechanical processes involved is known. Typically, experimental measurements are available that define an envelope of admissible states in some limited range of stress or strain space. This is often referred to as the failure surface. Points lying in the interior of the domain enclosed by the failure surface define states that do not lead to damage evolution in the material. In some situations, it is also possible to characterize the changes in shape experienced by the failure surface under sustained loading. This limited information is often all that is known about the damage in the material beyond some general conjectures about the actual physical mechanisms taking place.

For brittle materials such as ceramics, glasses, rocks or plain concrete, the latter being the case of interest here, the stress response can be characterized via linear elastic stress-strain relations. Damage in these materials is reflected at the macroscopic level in the progressive degradation experienced by the elastic moduli under sustained tensile loading, at states lying on (or above) the failure surface. The key piece of additional information needed to construct a complete constitutive model is an evolution law that characterizes this degradation process; i.e, a *damage rule*. The pioneering work of KACHANOV [1958] furnishes the first example of a damage rule, restricted in principle to either one-dimensional or isotropic theories, via the concept of effective stress. Proposals aimed at generalizing this original idea to account for anisotropy often introduce a fourth order tensor that maps between the stress and effective stress spaces, see e.g., LEMAITRE [1992] for a review of the extensive literature on this subject. The precise identification of this tensor in actual materials, plain concrete in particular, appears not to be readily accomplishable.

The purpose of this paper is to address in detail continuum and computational issues involved in the modeling of brittle materials, specifically in plain concrete, by exploiting an alternative framework that yields a fully anisotropic damage rule free from adjustable parameters. This approach employs an internal variable formalism that relies on two phenomenological assumptions which, in a sense, make up for our lack of detailed information on the micromechanics leading to damage evolution.

i. The choice of the elastic moduli as the set of internal (damage) variables. The idea of adopting the elastic moduli themselves or, equivalently, the compliance tensor as internal variables first appears in ORTIZ [1985] and SIMO & JU [1987].

ii. The principle of maximum (damage) dissipation. This single hypothesis automatically renders a fully anisotropic damage evolution law for the tensor of elastic moduli which, as alluded to above, is free from any adjustable parameters. The use of the principle of maximum dissipation as a means of uniquely defining the damage rule first appears in SIMO & JU [1987].

It should be noted that the second hypothesis is also the basis for the classical model of associative plasticity. In this context, assumption **ii** is often credited to von Mises

(see HILL [1983]) and is known as the principle of maximum plastic work. The continuum model so constructed, therefore, furnishes the counterpart in continuum damage mechanics of associative plasticity; and importantly it is completely defined once a failure surface is specified. Additionally, it is pointed out that assumption **ii** is also known to be valid in the disparate area of the modeling of damage due to Mullins' effect (GOVINDJEE & SIMO [1992]).

As in the case of softening plasticity, damage degradation of the elastic moduli leads to strain softening and, therefore, leads inevitably to the appearance of strongly discontinuous solutions; see BAŽANT & BELYTSCHKO [1985]. The underlying mechanism can be traced back to a local loss of Hadamard's strong ellipticity condition, see e.g. SLUYS [1992] for one of many derivations of this well-known fact, which typically takes place on sets of zero measure (BAŽANT & BELYTSCHKO [1985]). As a result, rate-independent models exhibiting softening render ill-posed the boundary value problems for the quasi-static case (or the initial boundary value problems in the dynamic case). In simulations, lack of well-posedness manifests itself in numerical solutions exhibiting a strong mesh–dependence. Motivated in part by these undesirable features, a number of authors (e.g., READ & HEGEMIER [1984]) have questioned the common point of view which regards loss of stiffness as a true material property of a continuum.

A number of techniques have been proposed to circumvent the preceding difficulties, from the early approaches of PIETRUSZCZAK & MRÓZ [1981] or BAŽANT & OH [1983] based on the use of a characteristic length to more recent methodologies that introduce a "regularization parameter." Representative examples of the latter approach are the viscous regularization, advocated in NEEDLEMAN [1987] and others, and regularization techniques based on the use of generalized continuum, as in SCHREYER [1990] or DEBORST [1991]. An alternative approach that retains the rate–independent character of the softening model and restores well-posedness, without resorting to a characteristic length, is described in SIMO, OLIVER & ARMERO [1993]. Since the emphasis in this paper is placed on modeling issues, amongst the many proposed techniques, only two methods are considered in detail: the viscous regularization and the characteristic length method in the form given in OLIVER [1989]. The goal here is to illustrate how existing regularization approaches fit within the proposed framework.

An outline of the remainder of this paper is as follows: In Section 2 we summarize the continuum framework for the design of continuum damage models based on assumptions **i** and **ii**, following the original presentation given in SIMO [1988a]. In Section 3 we consider in some detail computational issues involved in the implementation of the general model. These include, numerical integration, inclusion of rate effects and an alternative implementation of the concept of characteristic length. Section 4 describes in detail the formulation of an anisotropic continuum damage model model for the tensile cracking of concrete. A set of three simple damage surfaces are postulated for concrete which together with the damage evolution formulation of Section 2 renders a set of anisotropic evolution laws for the rank 4 stiffness tensor of the material and a set of softening variables. These evolution laws are then integrated using the algorithmic formulation of Section 3 and placed within a finite element code. Example calculations are shown to demonstrate various features of the model and to establish comparisons with available experimental data. These examples

demonstrate the full three–dimensional anisotropic features inherent in the model.

§2. Summary of the General Model

Consider a continuum solid occupying a region $\mathsf{B} \subset \mathsf{R}^3$. Since the interest here is in brittle materials, the deformation of the solid is well described by the linear strain theory and the assumption is made that no permanent (plastic) strains remain in the solid upon unloading. It follows that the stress state is characterized via the stress-strain relations:

$$\boldsymbol{\sigma} = \mathbb{C}:\boldsymbol{\epsilon}, \tag{2.1}$$

where $\boldsymbol{\sigma}$ is the Cauchy stress tensor, $\boldsymbol{\epsilon}$ is the infinitesimal strain tensor, and $\mathbb{C}$ is the rank 4 stiffness tensor of the material. To account for damage degradation in the material, the tensor $\mathbb{C}$ at time t is considered to be a function of the deformation history up to time t. According to the discussion in the introduction, it is further assumed that the elastic domain or admissible stress states is the set defined by M functions ϕ_k as

$$\mathsf{E}_\sigma = \{\boldsymbol{\tau} \in \mathsf{S} |\ \phi_k(\boldsymbol{\tau}, q) \leq 0 \quad (k = 1, ..., M)\}. \tag{2.2}$$

In this description, S stands for the set of symmetric rank 2 tensors and q is viewed as an internal variable that determines the evolution in time of the shape of the admissible set with progressive damage. The functions ϕ_k are assumed to be given from either experimental data or physical arguments about the material under consideration. An example of damage criterion suitable for brittle materials such as plain concrete is the Rankine condition.

Without any further information on the detailed micromechanics governing damage evolution, a unique damage rule can be specified by introducing the additional assumption of maximum damage dissipation, as follows. The first step is to regard the elastic moduli themselves as internal variables, leading to a free energy function for the material of the form

$$\Psi(\boldsymbol{\epsilon}, \mathbb{C}, \alpha) = \tfrac{1}{2}\boldsymbol{\epsilon}:\mathbb{C}:\boldsymbol{\epsilon} + S(\alpha), \tag{2.3}$$

where α is the internal variable conjugate to q, in the sense that $q = -\partial_\alpha S(\alpha)$. Use of the Legendre transformation yields the dual of (2.3), involving the stress field $\boldsymbol{\sigma}$ and the internal variable q, which is the starting point in ORTIZ [1985]. Equation (2.3), on the other hand, is taken as a point of departure in SIMO & JU [1987]. The first term in (2.3) represents the elastic free energy in the system while the second term is the free energy associated with the progressive degradation of the material. Degradation in brittle materials is usually induced by microcracking.

The second step in the analysis involves the enforcement of maximum damage dissipation. Recall that in the absence of thermal effects, the internal dissipation $\mathcal{D}$ is given by (TRUESDELL & NOLL [1965])

$$\mathcal{D} := -\dot{\Psi} + \boldsymbol{\sigma}:\dot{\boldsymbol{\epsilon}} \geq 0\ , \tag{2.4}$$

where superposed dots indicate ordinary time differentiation. Explicitly carrying out the time differentiation for the assumed form of the free energy (2.3), enforcing the stress-strain relations (2.1) and inserting the expression $q = -\partial_\alpha S(\alpha)$ yields

$$\mathcal{D} = \tfrac{1}{2}\boldsymbol{\sigma}:\dot{\mathbb{D}}:\boldsymbol{\sigma} + q\dot{\alpha} \geq 0, \tag{2.5}$$

where $\mathbb{D} = \mathbb{C}^{-1}$ denotes the material compliance tensor. The hypothesis of maximum dissipation states that among all admissible states lying in $\mathbb{E}_\sigma$, the actual state of stress in the solid is the one which maximizes (2.5). For materials that exhibit softening, this hypothesis is not strictly enforced. Instead, the hypothesis is reduced to finding the critical point of dissipation since no such maximum exists. To perform this constrained optimization problem one first constructs the associated Lagrangian

$$\mathcal{L}(\boldsymbol{\sigma}, q) = -\mathcal{D} + \sum_{k=1}^{M} \gamma_k \phi_k \,, \tag{2.6}$$

where $\gamma_k \geq 0$ are known as generalized Lagrange multipliers or consistency parameters. The critical point of this Lagrangian is characterized by the classical optimality conditions (see e.g. LUENBERGER, §10.8 [1984]):

$$\left.\begin{aligned} \partial_\sigma \mathcal{L} = \mathbf{0}, \quad \partial_q \mathcal{L} = 0, \\ \phi_k \leq 0, \quad \gamma_k \geq 0 \quad \text{and} \quad \textstyle\sum_{k=1}^{M} \gamma_k \phi_k = 0. \end{aligned}\right\} \tag{2.7}$$

Denoting by $\otimes$ the tensor (or outer) product symbol, conditions (2.7) result in the damage flow/evolution rules

$$\dot{\mathbb{D}} = \sum_{k=1}^{M} \gamma_k \frac{\partial_\sigma \phi_k \otimes \partial_\sigma \phi_k}{\partial_\sigma \phi_k : \boldsymbol{\sigma}} \quad \text{and} \quad \dot{\alpha} = \sum_{k=1}^{M} \gamma_k \partial_q \phi_k \tag{2.8}$$

supplemented by the Kuhn-Tucker unilateral constraint conditions $(2.7)_2$, i.e.,

$$\phi_k \leq 0, \quad \gamma_k \geq 0 \quad \text{and} \quad \sum_{k=1}^{M} \gamma_k \phi_k = 0. \tag{2.9}$$

Relations (2.9) give precise conditions for assessing active damage evolution (loading) or inactive damage (elastic unloading) in the material. Their significance is identical to the loading/unloading conditions for multi-surface plasticity in the form first stated in KOITER [1953] and necessitate, therefore, no further elaboration. In a strict sense, the damage rules and the derivation sketched above are valid if the constraints are of the form $\phi_k(\boldsymbol{\sigma}, q) = f_k(\boldsymbol{\sigma}) - h_k(q)$, with $f_k(\boldsymbol{\sigma})$ homogeneous of degree one. This is a situation often encountered in practice and, in particular, is the case of interest discussed in Section 4.

To carry one step further the formal analogy with classical plasticity, observe that Equations (2.8) and (2.1) imply the following expression for the time rate of change of stress:

$$\dot{\boldsymbol{\sigma}} = \mathbb{C}:\left[\dot{\boldsymbol{\epsilon}} - \sum_{k=1}^{M} \gamma_k \partial_\sigma \phi_k\right]. \tag{2.10}$$

The structure of this expression is essentially identical to that arising in the classical model of associative plasticity, although its physical interpretation is quite different. In (2.10), the "added" strain contribution arises from loss of stiffness in the material whereas the analogous term in plasticity theory is due to the change in permanent (plastic) strains at a constant stiffness. It is a straightforward matter to formally combine these two mechanisms and arrive at a phenomenological model that incorporates both damage degradation and permanent (residual) strains. Such a task, however, will not be pursued here.

Table 1. Rate Independent, Anisotropic Damage Model

Free energy [with elastic moduli $\mathbb{C}$ and compliance tensor $\mathbb{D} = \mathbb{C}^{-1}$]:

$$\Psi(\boldsymbol{\varepsilon}, \mathbb{C}, \alpha) = \tfrac{1}{2}\boldsymbol{\varepsilon}\colon\mathbb{C}\colon\boldsymbol{\varepsilon} + S(\alpha).$$

Stress-strain and internal variable relations:

$$\boldsymbol{\sigma} = \mathbb{C}\colon\boldsymbol{\varepsilon} \quad \text{and} \quad q = -\partial_\alpha S.$$

Damage rule for compliance tensor and internal variable:

$$\dot{\mathbb{D}} = \sum_{k=1}^{M} \gamma_k \frac{\partial_\sigma \phi_k \otimes \partial_\sigma \phi_k}{\partial_\sigma \phi_k\colon\boldsymbol{\sigma}} \quad \text{and} \quad \dot{\alpha} = \sum_{k=1}^{M} \gamma_k \partial_q \phi_k.$$

Kuhn-Tucker damage/no-damage conditions:

$$\phi_k(\boldsymbol{\sigma}, q) \le 0, \quad \gamma_k \ge 0 \quad \text{and} \quad \sum_{k=1}^{M} \phi_k(\boldsymbol{\sigma}, q)\gamma_k = 0.$$

Consistency condition: $\sum_{k=1}^{M} \dot{\phi}_k(\boldsymbol{\sigma}, q)\gamma_k = 0.$

For completeness, the rate independent constitutive equations are summarized in Table 1 above. As these equations stand, however, the the resulting model will yield an ill-posed initial boundary value problem if the material exhibits softening. A brief discussion of the issues involved is given in Section 2.2 below.

2.1. Rate Effects.

For materials that display rate effects, the model summarized in Table 1 can be easily extended to incorporate first order rate dependencies. For single surface models (i.e., $k = 1$), the extension is patterned after the Prager-Perzyna model of viscoplasticity, and amounts to replacing the Kuhn–Tucker optimality loading/unloading conditions by the constitutive equation:

$$\gamma_k = \frac{< \phi_k >}{\eta}, \tag{2.11}$$

where $< \cdot >= \frac{1}{2}[(\cdot) + |\cdot|]$ is known as the Macauley bracket and η is a scalar governing the viscosity of the relaxation process. For hardening materials, it is well-known that as $\eta \to 0$ the rate independent solution is recovered. Whether the same property holds for softening materials is an open question. The widespread use of the viscoplastic regularization as a means of circumventing ill-posedness of the rate–independent problem rests on the belief that this is *not* the case.

Remark 2.1.

Difficulties arise in the generalization of (2.11) to the case of an elastic domain defined by $M > 1$ intersecting surfaces, unless further restrictions are placed on the gradients $\partial_\sigma \phi_k$ of the constraints; see SIMO, KENNEDY, & GOVINDJEE [1988] for additional details. In particular, the conditions set forth in this latter reference show that the inviscid limit is well–behaved (for hardening materials) if the gradients are stiffness–orthogonal, i.e. if

$$\partial_\sigma \phi_k : \mathbb{C} : \partial_\sigma \phi_j = 0 \tag{2.12}$$

for $j \neq k$. This observation will prove useful in the rate-dependent extension of the model described in Section 4. □

2.2. Dissipation and Characteristic Lengths.

Equations like those in Table 1 are well known to produce ill-posed initial boundary value problems when the elastic domain defined in Equation (2.2) contracts with the evolution of the internal variables q. The severe difficulties associated with lack of well-posedness are quite different from those arising from global lack of uniqueness of the initial boundary value problem (see DEBORST [1987] for an illustration of these latter difficulties). READ & HEGEMIER [1984], for instance, have advanced a physical mechanism that correlates "ill-posedness" of conventional softening models with attempts to model a structural response as a continuum response, thus suggesting the introduction of a length scale in the problem. From a purely mechanical standpoint, a source of difficulty in the model in Table 1 lies in the expression for the dissipation, which is intrinsically defined per unit volume and given by Equation (2.5). Typically, however, for brittle materials the dissipation mechanism is the generation of cracks. Such a mechanism dissipates energy on a per unit area basis. Hence the model derived above and the physical mechanism are incompatible in their basic length scales.

As pointed out in the introduction, a number of approaches can be found in the literature that introduce a length scale into the model in an attempt to resolve the inconsistency between the model and the physical mechanism. A review of the main methods currently employed can be found in SLUYS [1992]; these include higher order gradient theories, rate effect theories, Cosserat theories, and direct characteristic length theories. The use of higher order gradient or Cosserat methods requires strict physical justification because of their increased complexity over the two other approaches mentioned. The inclusion of rate effects as described above provides for one rather simple method of introducing an implicit length scale into the formulation. This method, however, is lacking in several respects. One, in the limit of the rate independent model, the equations may once again produce ill-posed initial boundary value problems. Two, the viscosity parameter governs

both the rate characteristics of the material as well as the characteristic length of the material; see SLUYS [1992]. These two phenomena should, however, be governed by separate parameters as they are separate physical mechanisms that are not intimately associated with each other in general. Note also that in an algorithmic setting there may be time step restrictions on otherwise "unconditionally stable" integration algorithms in order to maintain the "well-posedness" of the problem (SIMO [1988b]). Finally, no conclusive proof currently exists on the effectiveness of this approach other than experience gained in numerical simulations. Direct characteristic length methods, on the other hand, require a reasonable understanding of the physical cause of the material's degradation; in the case of brittle materials, this information is often available.

An example of a direct characteristic length theory is that of OLIVER [1989]. In this theory, a dissipation constraint is used to enforce a desired amount of dissipation in a volume of material with a single crack growing through it. The appeal of this construction lies in its theoretical and computational simplicity over, perhaps, more correct but also more complex approaches such as the non-local damage theory of PIJAUDIER-CABOT & BAŽANT [1987] or Cosserat theories as in DEBORST [1991]. The basic idea is that, if the fracture energy per unit area crack advance G_f is a known material property, then the energy dissipated per unit volume g_f in the continuum theory is related through the expression

$$g_f = G_f / l^* , \tag{2.13}$$

where l^* is know as the characteristic length and is given as the reciprocal of the directional derivative of the crack indicator function in the direction of the crack plane normal; see OLIVER [1989] for more details. Equation (2.13) provides a practical restriction on the softening properties of the model. This is seen to be the case since

$$g_f = \int_\Gamma \mathcal{D}\, d\Gamma , \tag{2.14}$$

where the path of integration Γ in (2.14) is from a state of no damage to a state of total failure. Equation (2.14) involves the softening properties of the model through the dissipation rate $\mathcal{D}$ and hence together with (2.13) provides a restriction on the softening parameters of the material. Note that since (2.14) is a path dependent integral the path chosen must correspond to that used to experimentally determine G_f. An application of this method is shown in Section 4.

A completely different approach based on the mathematical analysis of the discontinuous solutions that arise in the presence of softening is described in SIMO, OLIVER & ARMERO [1993]. The "regularized" softening model strictly remains rate–independent and the initial boundary value problem becomes well-posed, leading to numerical solutions exhibiting no mesh-dependence whatsoever. The notion of a characteristic length plays no role in this approach at the continuum level. The results of this analysis provide a partial justification for the preceding methodology.

§3. Computational Issues

Because of the nonlinear nature of the equations in Table 1, numerical methods are usually employed when using them to solve initial boundary value problems. The discussion that follows is restricted to their use in the standard strain driven framework that exists in most finite element codes — whether globally performing load or displacement controlled calculations. This framework assumes that the strain $\boldsymbol{\varepsilon}^n$, the stiffness $\mathbb{C}^n$, and the internal variables α^n are all known at time t^n. In addition, it is assumed that the strain $\boldsymbol{\varepsilon}^{n+1}$ at time $t^{n+1} > t^n$ is known and that the stresses and values of the stiffness and internal variables at time t^{n+1} are desired. In what follows, superscript n's and $n+1$'s will always denote quantities evaluated at times t^n and t^{n+1} respectively.

3.1. Return Mapping Algorithm.

The method of solving for the desired unknowns parallels very closely the so-called return mapping algorithms of classical plasticity (see the comprehensive review in SIMO [1993]). The only substantial difference lies in the details of the consistency parameter calculation when softening is involved, as will be seen in Section 4. To begin, the flow rules for the compliance tensor and the internal variables are integrated using the implicit backward Euler rule. This results in the following two expressions:

$$\mathbf{D}^{n+1} = \mathbf{D}^n + \sum_{k=1}^{M} \Delta\gamma_k \frac{\partial_\sigma \phi_k^{n+1} \otimes \partial_\sigma \phi_k^{n+1}}{\partial_\sigma \phi_k^{n+1} : \boldsymbol{\sigma}^{n+1}} \tag{3.1}$$

$$\alpha^{n+1} = \alpha^n + \sum_{k=1}^{M} \Delta\gamma_k \partial_q \phi_k^{n+1}\,, \tag{3.2}$$

where $\Delta\gamma_k \geq 0$ is a discrete consistency parameter. Note that Equation (3.1) can be inverted using the Sherwin-Morrison-Woodbury formula (see for example DENNIS & SCHNABEL §8.3 [1983]) to the give the stiffness tensor at time t^{n+1}.

Equation (3.1) can now be combined with the stress-strain relation (2.1) at time t^{n+1} to give an implicit expression for the current value of the stress tensor as

$$\boldsymbol{\sigma}^{n+1} = \mathbb{C}^n : [\boldsymbol{\varepsilon}^{n+1} - \sum_{k=1}^{M} \Delta\gamma_k \partial_\sigma \phi_k^{n+1}]\,. \tag{3.3}$$

The expression for the current values of the internal stresses is simply

$$q^{n+1} = -\partial_\alpha S(\alpha^{n+1})\,. \tag{3.4}$$

We now require the Kuhn-Tucker damage/no-damage conditions (2.9) to be satisfied at time t^{n+1}; i.e. for $(k = 1, ..., M)$:

$$\phi_k^{n+1} \leq 0, \quad \Delta\gamma_k \geq 0 \quad \text{and} \quad \sum_{k=1}^{M} \phi_k^{n+1} \Delta\gamma_k = 0. \tag{3.5}$$

Thus at the end of every time step in a calculation the constraints on the admissible stress states are always satisfied. Further examination of Equations (3.1)–(3.5) results in the

observation that, just as in the time continuous case, when $\phi_k^{n+1} < 0$, then $\Delta\gamma_k = 0$ and no damage evolution takes place with respect to the k^{th} damage surface. Algorithmically, this motivates the notion of a trial "elastic" predictor state defined by $\Delta\gamma_k = 0$ for all k. The trial stress is given by

$$\boldsymbol{\sigma}_{\text{trial}}^{n+1} = \mathbb{C}^n : \boldsymbol{\varepsilon}^{n+1} \tag{3.6}$$

and the trial internal stresses are given by

$$q_{\text{trial}}^{n+1} = q^n \,. \tag{3.7}$$

A "predictor–corrector" type algorithm can now be defined as:

1. For each k check whether $\phi_k(\boldsymbol{\sigma}_{\text{trial}}^{n+1}, q_{\text{trial}}^{n+1}) \leq 0$. If so, then assume the surface is inactive and set $\Delta\gamma_k = 0$.
2. If $\phi_k(\boldsymbol{\sigma}_{\text{trial}}^{n+1}, q_{\text{trial}}^{n+1}) > 0$, then assume the surface is active and that $\Delta\gamma_k > 0$.
3. If all the surfaces are inactive, then

$$\begin{aligned} \boldsymbol{\sigma}^{n+1} &= \boldsymbol{\sigma}_{\text{trial}}^{n+1} \\ q^{n+1} &= q_{\text{trial}}^{n+1} \\ \alpha^{n+1} &= \alpha^n \\ \mathbb{D}^{n+1} &= \mathbb{D}^n \end{aligned} \tag{3.8}$$

   and the state of the system at time t^{n+1} is fully defined.
4. If any of the surfaces are active, then use the consistency conditions that $\phi_k^{n+1} = 0$ for $k \in \{\text{active surfaces}\}$ and Equations (3.1)–(3.4) to simultaneously solve for the unknowns, $\Delta\gamma_k$, $\boldsymbol{\sigma}^{n+1}$, and q^{n+1}, and then update the other state variables α^{n+1} and $\mathbb{D}^{n+1}$.

Remark 3.1.

When the orthogonality condition (2.12) is not met, a fifth step must be added to algorithm to insure that the proper set of active surfaces was chosen. For further details see SIMO, KENNEDY, & GOVINDJEE [1988]. □

Remark 3.2.

In general, these equations form an intractable highly nonlinear system of equations that must be simultaneously solved for the unknowns; however, for a certain class of popular damage surfaces this nonlinearity is tractable from the standpoint of practical calculations. Consider the case of a single active damage surface of the form

$$\phi(\boldsymbol{\sigma}, q) = f(\boldsymbol{\sigma}) - \sigma_f + q = 0 \,, \tag{3.9}$$

where σ_f is a scalar constant and the internal stress q is also a scalar. In this case, Equations (3.3)-(3.4) reduce to

$$\boldsymbol{\sigma}^{n+1} = \boldsymbol{\sigma}_{\text{trial}}^{n+1} - \Delta\gamma \mathbb{C}^n : \partial_\sigma f(\boldsymbol{\sigma}^{n+1}) \tag{3.10}$$

$$q^{n+1} = -\partial_\alpha S(\alpha^n + \Delta\gamma) \,. \tag{3.11}$$

By substituting Equation (3.11) into (3.9), one obtains an equation in terms of $\boldsymbol{\sigma}^{n+1}$ and $\Delta\gamma$. This equation together with Equation (3.10) forms a complete set of equations that may solved for the unknowns $\boldsymbol{\sigma}^{n+1}$ and $\Delta\gamma$. In the case where $\partial_\sigma f$ is a constant the system of equations reduces even further into a single (in general nonlinear) equation for the scalar $\Delta\gamma$. These arguments also hold true for the case of multiple damage surfaces. □

3.2. Rate Dependent Model.

The development of the algorithm for the rate dependent case exactly mimics the rate independent case. The viscoplastic flow rules are first integrated with a backward Euler difference scheme to give

$$\mathbf{D}^{n+1} = \mathbf{D}^n + \sum_{k=1}^{M} \frac{<\phi_k^{n+1}> \Delta t}{\eta} \frac{\partial_\sigma \phi_k^{n+1} \otimes \partial_\sigma \phi_k^{n+1}}{\partial_\sigma \phi_k^{n+1} : \boldsymbol{\sigma}^{n+1}} \tag{3.12}$$

$$\alpha^{n+1} = \alpha^n + \sum_{k=1}^{M} \frac{<\phi_k^{n+1}> \Delta t}{\eta} \partial_q \phi_k^{n+1}, \tag{3.13}$$

where $\Delta t = t^{n+1} - t^n$. The stress at time t^{n+1} can now be written as

$$\boldsymbol{\sigma}^{n+1} = \mathbb{C}^n : \left[\boldsymbol{\varepsilon}^{n+1} - \sum_{k=1}^{M} \frac{<\phi_k^{n+1}> \Delta t}{\eta} \partial_\sigma \phi_k^{n+1} \right]. \tag{3.14}$$

The internal stress expression (3.4) with α^{n+1} now given by Equation (3.13) also holds.

For the rate dependent problem there are no Kuhn-Tucker conditions but one can still use an algorithm that is similar to the one defined for the rate independent case. This follows because Equations (3.12) and (3.13) indicate that damage evolution does not take place with respect to the k^{th} surface unless $\phi_k > 0$. Thus the following algorithm can be defined:

1. For each k check whether $\phi_k(\boldsymbol{\sigma}_{\text{trial}}^{n+1}, q_{\text{trial}}^{n+1}) \leq 0$. If so, then assume the surface is inactive and set $\frac{<\phi_k^{n+1}>\Delta t}{\eta} = 0$.
2. If $\phi_k(\boldsymbol{\sigma}_{\text{trial}}^{n+1}, q_{\text{trial}}^{n+1}) > 0$, then assume the surface is active and that $\frac{<\phi_k^{n+1}>\Delta t}{\eta} > 0$.
3. If all the surfaces are inactive, then

$$\begin{aligned} \boldsymbol{\sigma}^{n+1} &= \boldsymbol{\sigma}_{\text{trial}}^{n+1} \\ q^{n+1} &= q_{\text{trial}}^{n+1} \\ \alpha^{n+1} &= \alpha^n \\ \mathbf{D}^{n+1} &= \mathbf{D}^n \end{aligned} \tag{3.15}$$

   and the state of the system at time t^{n+1} is fully defined.
4. If any of the surfaces are active, use the damage surface equations ϕ_k^{n+1} for $k \in$ {active surfaces} and Equations (3.12)–(3.14) and (3.4) to simultaneously solve for $\frac{<\phi_k^{n+1}>\Delta t}{\eta}$, $\boldsymbol{\sigma}^{n+1}$, and q^{n+1}, and then update the remaining state variables.

Remark 3.3.

For the general case, it is seen that the main difference between the rate dependent and rate independent case is that $\Delta\gamma_k$ has been replaced by $\frac{<\phi_k^{n+1}>\Delta t}{\eta}$. The other difference lies in the fact that $\phi_k^{n+1} \neq 0$ for $k \in \{\text{active surfaces}\}$ in the rate dependent case. However, since $\phi_k^{n+1} > 0$ for $k \in \{\text{active surfaces}\}$, one can write the analog to the rate independent equation $\phi_k^{n+1} = 0$ as

$$-\left(\frac{\eta}{\Delta t}\right)\left[\frac{<\phi_k^{n+1}>\Delta t}{\eta}\right] + \phi_k(\boldsymbol{\sigma}^{n+1}, q^{n+1}) = 0\,. \tag{3.16}$$

Note that in Equation (3.16) the quantity $\frac{<\phi_k^{n+1}>\Delta t}{\eta}$ is considered as one variable to be solved for; therefore, in the limit as $\eta \to 0$ the rate independent case is recovered (assuming the orthogonality condition (2.12) is satisfied). This observation also makes it possible to use the same solver code for both cases by always using (3.16) in the iteration process. □

3.3. Characteristic Length.

In conjunction with the algorithms outlined above, an algorithm for calculating the characteristic length is needed. The discussion that follows pertains to the method proposed by OLIVER [1989] and is restricted to the context of isoparametric C^0 finite elements. Recall, first, OLIVER'S algorithm for calculating the characteristic length, l^*:

$$(l^*)^{-1} = \partial_x \tau \cdot \boldsymbol{n} = \left[\sum_{A=1}^{N_{\text{nodes}}} \partial_x N_A(\boldsymbol{x}) \tau_A\right] \cdot \boldsymbol{n}(\boldsymbol{x})\,, \tag{3.17}$$

where $N_A(\cdot)$ are the element shape functions, N_{nodes} is the number of element nodes, τ_A are the nodal values of the *crack indicator* function τ, and $\boldsymbol{n}(\boldsymbol{x})$ is the normal to the smeared crack plane at a point $\boldsymbol{x}$. According to OLIVER'S definition, the *crack indicator* function should take the value of 1 in front of the crack field and 0 behind the crack field. Front and back are determined by the following relation

$$\tau_A = \begin{cases} 1 & (\boldsymbol{x}_A - \boldsymbol{x}_c) \cdot \boldsymbol{n}(\boldsymbol{x}) > 0 \\ 0 & (\boldsymbol{x}_A - \boldsymbol{x}_c) \cdot \boldsymbol{n}(\boldsymbol{x}) \leq 0\,, \end{cases} \tag{3.18}$$

where $\boldsymbol{x}$ represents the point in the body where one is trying to evaluate the characteristic length, $\boldsymbol{x}_A$ is the nodal coordinate, and $\boldsymbol{x}_c$ represents the center of element in which $\boldsymbol{x}$ lies. In the context of 2-D problems examined by OLIVER, Equation (3.18) is adequate. However, for 3-D problems using the common 8-noded C^0 brick element Equation (3.18) leads to a discontinuous characteristic length function (3.17). This can best be seen by considering an example. Consider the 8-noded C^0 brick in the isoparametric domain where points are denoted by $\boldsymbol{\xi} = (\xi_1, \xi_2, \xi_3)$. In this case,

$$(l^*)^{-1} = \partial_x \tau \cdot \boldsymbol{n} = \|(\partial_x \boldsymbol{\xi})\boldsymbol{n}\| \sum_{A=1}^{N_{\text{nodes}}} \tau_A \partial_\xi N_A(\boldsymbol{\xi}) \cdot \bar{\boldsymbol{n}}\,. \tag{3.19}$$

In (3.19), $\bar{\boldsymbol{n}} = (\partial_x \boldsymbol{\xi})\boldsymbol{n}/\|(\partial_x \boldsymbol{\xi})\boldsymbol{n}\|$ which by construction is of unit norm; hence $\bar{\boldsymbol{n}}$ can be completely defined by a set of two angles (θ, φ) with respect to the isoparametric coordinate frame; see Figure **1**. Doing so allows one to write

$$\bar{\boldsymbol{n}} = \left\{ \begin{array}{c} \cos\theta \sin\varphi \\ \sin\theta \sin\varphi \\ \cos\varphi \end{array} \right\} . \tag{3.20}$$

Equation (3.19) is now evaluated for two cases that should produce characteristic length values arbitrarily close to each other. For case 1, $(\theta, \varphi) = (\frac{\pi}{2}, \frac{\pi}{4} + \epsilon)$ where $\epsilon << 1$. This implies by (3.18), that $\tau_3 = \tau_4 = \tau_7 = \tau_8 = 1$ and $\tau_1 = \tau_2 = \tau_5 = \tau_6 = 0$ when using a standard node numbering scheme as shown in Figure **2**. The second case corresponds to $(\theta, \varphi) = (\frac{\pi}{2} + \delta, \frac{\pi}{4} + \epsilon)$ for arbitrarily small but positive δ. In this case, $\tau_4 = \tau_5 = \tau_7 = \tau_8 = 1$ and $\tau_1 = \tau_2 = \tau_3 = \tau_6 = 0$; see Figure **3**.

If (3.19) is to be continuous with respect to the orientation of the crack field then cases 1 and 2 should produce virtually the same result within a small tolerance that is a function of δ. For case 1, Equation (3.19) gives

$$\partial_x \tau \cdot \boldsymbol{n} = \|(\partial_x \boldsymbol{\xi})\boldsymbol{n}\| \frac{1}{2} \sin\theta \sin\varphi \approx \|(\partial_x \boldsymbol{\xi})\boldsymbol{n}\| \frac{\sqrt{2}}{4} . \tag{3.21}$$

For case 2, Equation (3.19) gives

$$\partial_x \tau \cdot \boldsymbol{n} = \|(\partial_x \boldsymbol{\xi})\boldsymbol{n}\| \frac{1}{4} (\sin\theta \sin\varphi + \cos\varphi)(1 + \xi_1 \xi_3) . \tag{3.22}$$

Only when $\xi_1 \xi_3 = 0$, does (3.22) reduce to (3.21). If one assumes that a full quadrature rule is being used and tries to evaluate the characteristic length at the Gauss points $(\pm\frac{1}{\sqrt{3}}, \pm\frac{1}{\sqrt{3}}, \pm\frac{1}{\sqrt{3}})$, then Equation (3.22) reduces to

$$\partial_x \tau \cdot \boldsymbol{n} \approx \|(\partial_x \boldsymbol{\xi})\boldsymbol{n}\| \frac{\sqrt{2}}{4} (1 \pm \frac{1}{3}) , \tag{3.23}$$

where the sign in $(1 \pm \frac{1}{3})$ depends upon the Gauss point chosen. Clearly (3.23) does not tend to (3.21) in the limit of vanishing δ.

It is observed that the difficulty that arises is due to the discontinuous nature of the definition of the nodal values for the crack indicator function. To circumvent this difficulty, a simple continuous definition for τ_A can be made as follows:

$$\tau_A = \frac{(\boldsymbol{x}_A - \boldsymbol{x}_c) \cdot \boldsymbol{n}(\boldsymbol{x}) - \tau^{\min}}{\tau^{\max} - \tau^{\min}} , \tag{3.24}$$

where

$$\tau^{\min} = \min_{A=1, N_{\text{nodes}}} \{(\boldsymbol{x}_A - \boldsymbol{x}_c) \cdot \boldsymbol{n}(\boldsymbol{x})\} \tag{3.25}$$

$$\tau^{\max} = \max_{A=1, N_{\text{nodes}}} \{(\boldsymbol{x}_A - \boldsymbol{x}_c) \cdot \boldsymbol{n}(\boldsymbol{x})\} . \tag{3.26}$$

The redefinition of (3.18) as (3.24) removes the continuity problems noted above and yet remains faithful to the original idea proposed by OLIVER.

§4. Application: Concrete

In this section, an application is made of the developments of Sections 2 and 3. The example problem to be considered is the brittle tensile failure of concrete. Failure in the material is assumed to initiate when the 1st principal stress in the material exceeds some threshold value. In the discussion that follows, the principal direction associated with this principal stress is assumed known and given by the eigenvector $\boldsymbol{n}$. This vector defines the normal to a "smeared" crack field that is locally fixed in the material after initiation. Across this smeared crack field, tensile tractions are limited by some critical value that decreases exponentially with increasing deformation. Likewise, shear tractions across the smeared crack field are limited by some critical value that decreases with increasing deformation. The progressive degradation of strength as employed here is a generalization of the original smeared crack model of RASHID [1968] and represents the more modern viewpoint that the degradation is progressive; see e.g. DEBORST & NAUTA [1985].

4.1. Damage Surfaces.

To begin, a set of damage surfaces must be defined. Based on the description above, three coupled surfaces are postulated — the first to control the tensile tractions across the smeared crack field and the second two to control the shear tractions across the smeared crack field:

$$\phi_1 = \boldsymbol{S}_1 : \boldsymbol{\sigma} - f_n + k_n q \leq 0\,, \tag{4.1}$$

$$\phi_2 = |\boldsymbol{S}_2 : \boldsymbol{\sigma}| - f_s + k_s q \leq 0\,, \tag{4.2}$$

$$\phi_3 = |\boldsymbol{S}_3 : \boldsymbol{\sigma}| - f_s + k_s q \leq 0\,. \tag{4.3}$$

In the above, $\boldsymbol{S}_1 = \boldsymbol{n} \otimes \boldsymbol{n}$, $\boldsymbol{S}_2 = \frac{1}{2}(\boldsymbol{n} \otimes \boldsymbol{m} + \boldsymbol{m} \otimes \boldsymbol{n})$, and $\boldsymbol{S}_3 = \frac{1}{2}(\boldsymbol{n} \otimes \boldsymbol{l} + \boldsymbol{l} \otimes \boldsymbol{n})$; $\boldsymbol{m}$ and $\boldsymbol{l}$ denote unit vectors that together with $\boldsymbol{n}$ form an orthonormal basis; f_n is the critical tensile traction that can be held across the smeared crack field; f_s is the critical shear traction that can be held across the smeared crack field; q is an internal scalar softening stress tending to f_n; and k_n and k_s are coupling constants that are chosen so that the tensile and shear tractions across the smeared crack field reach their asymptotic values simultaneously.

Theoretically, one would like to choose $k_n = 1$, however, for computational reasons it is better to choose $k_n = (1 - \beta_n)$ where β_n is a small number. The effect of this is to give the material a small amount of residual tensile strength. The constant k_s is set in a similar manner to $\frac{f_s}{f_n}(1 - \beta_s)$, where β_s represents the residual shear strength of the material. Ideally, this value would be pressure dependent, however, for simplicity this added complexity is avoided here. Additionally, the softening stress is assumed to be given by the following relationship:

$$q = f_n(1 - \exp[-H\alpha]) = -\partial_\alpha S\,, \tag{4.4}$$

where H is a softening decay constant that is determined by Equations (2.13) and (2.14). The motivation for this expression comes from the experimental observation of exponential type softening behavior.

4.2. Flow Rules and Consistency Parameters.

Using (4.1)-(4.3) in (2.8) gives the damage flow rules. By noting that $\partial_\sigma \phi_1 = \boldsymbol{S}_1$, $\partial_\sigma \phi_2 = \text{sign}(\boldsymbol{S}_2 : \boldsymbol{\sigma})\boldsymbol{S}_2$, and $\partial_\sigma \phi_3 = \text{sign}(\boldsymbol{S}_3 : \boldsymbol{\sigma})\boldsymbol{S}_3$, one has that

$$\dot{\mathbf{D}} = \gamma_1 \frac{\boldsymbol{S}_1 \otimes \boldsymbol{S}_1}{\boldsymbol{S}_1 : \boldsymbol{\sigma}} + \gamma_2 \frac{\boldsymbol{S}_2 \otimes \boldsymbol{S}_2}{|\boldsymbol{S}_2 : \boldsymbol{\sigma}|} + \gamma_3 \frac{\boldsymbol{S}_3 \otimes \boldsymbol{S}_3}{|\boldsymbol{S}_3 : \boldsymbol{\sigma}|} \tag{4.5}$$

$$\dot{\alpha} = k_n \gamma_1 + k_s \gamma_2 + k_s \gamma_3 \,. \tag{4.6}$$

Remark 4.1.

Flow rule (4.5) indicates that if the material is initially isotropic then the orthogonality condition (2.12) is satisfied. This follows since $\boldsymbol{S}_1 : \boldsymbol{S}_2 = \boldsymbol{S}_1 : \boldsymbol{S}_3 = \boldsymbol{S}_2 : \boldsymbol{S}_3 = 0$ and that $\boldsymbol{S}_1 : \mathbb{C}^0 : \boldsymbol{S}_2 = \boldsymbol{S}_1 : \mathbb{C}^0 : \boldsymbol{S}_3 = \boldsymbol{S}_2 : \mathbb{C}^0 : \boldsymbol{S}_3 = 0$ where $\mathbb{C}^0$ is the initial undamaged isotropic stiffness of the material. □

Utilizing the orthoganality condition and the consistency conditions, the consistency parameters are given by

$$\gamma_k = \sum_{j=1}^{3} g_{kj}^{-1} d_j \,, \tag{4.7}$$

where the vector

$$\boldsymbol{d} = \begin{Bmatrix} \boldsymbol{S}_1 : \mathbb{C} : \dot{\boldsymbol{\epsilon}} \\ \text{sign}(\boldsymbol{S}_2 : \boldsymbol{\sigma}) \boldsymbol{S}_2 : \mathbb{C} : \dot{\boldsymbol{\epsilon}} \\ \text{sign}(\boldsymbol{S}_3 : \boldsymbol{\sigma}) \boldsymbol{S}_3 : \mathbb{C} : \dot{\boldsymbol{\epsilon}} \end{Bmatrix} \tag{4.8}$$

and the matrix

$$\boldsymbol{g} = \begin{bmatrix} \boldsymbol{S}_1 : \mathbb{C} : \boldsymbol{S}_1 - k_n \partial_{\gamma_1} q & -k_n \partial_{\gamma_2} q & -k_n \partial_{\gamma_3} q \\ & \boldsymbol{S}_2 : \mathbb{C} : \boldsymbol{S}_2 - k_s \partial_{\gamma_2} q & -k_s \partial_{\gamma_3} q \\ \text{sym.} & & \boldsymbol{S}_3 : \mathbb{C} : \boldsymbol{S}_3 - k_s \partial_{\gamma_3} q \end{bmatrix} \tag{4.9}$$

where $\partial_{\gamma_1} q = k_n f_n H \exp(-H\alpha)$ and $\partial_{\gamma_2} q = \partial_{\gamma_3} q = k_s f_n H \exp(-H\alpha)$.

4.3. Dissipation Constraint.

For brittle materials like concrete, the fracture toughness (energy per unit crack advance) is usually measured under pure mode I conditions. Thus the expression for the dissipation that should be used in (2.14) is

$$\mathcal{D} = \frac{1}{2} \boldsymbol{\sigma} : \left[\gamma_1 \frac{\boldsymbol{S}_1 \otimes \boldsymbol{S}_1}{\boldsymbol{S}_1 : \boldsymbol{\sigma}} \right] : \boldsymbol{\sigma} + q\dot{\alpha} \,, \tag{4.10}$$

where all the shear terms have been assumed zero. Simplifying (4.10) with the aid of (4.1) and substituting into (2.14) gives

$$g_f = \int_\Gamma \frac{1}{2k_n} \dot{\alpha}(f_n - q) + q\dot{\alpha} \, d\Gamma \,. \tag{4.11}$$

The path of integration is from a state of no-damage, $\alpha = 0$, to a state of complete damage α_c. The state of complete damage is defined by $q(\alpha_c) = f_n$. However, in the present case there is no such state for finite α; see Eq. (4.4). Therefore, α_c is set as the value where q reaches a predefined fraction of its asymptotic limit. Equally, one could define α_c through the relation $H\alpha_c = \lambda$, where for instance a value of $\lambda = 4$ would correspond to a value of q within 2 percent of its asymptotic limit f_n. Doing so in (4.11) implies that

$$g_f = \frac{f_n}{H}\left[\lambda - \frac{2k_n - 1}{2k_n}(1 - \exp[-\lambda])\right] . \tag{4.12}$$

Thus, the softening decay constant is constrained by (2.13) to be

$$H = l^* \frac{f_n}{G_f}\left[\lambda - \frac{2k_n - 1}{2k_n}(1 - \exp[-\lambda])\right] . \tag{4.13}$$

4.4. Algorithmic Issues.

The algorithmic approximation of the above equations follows from Section 3. In particular note that Remark **3.2** applies to the postulated damage surfaces. For completeness the time integrated equations are given below. For the flow rules:

$$\mathbb{D}^{n+1} = \mathbb{D}^n + \Delta\gamma_1 \frac{\boldsymbol{S}_1 \otimes \boldsymbol{S}_1}{\boldsymbol{S}_1 : \boldsymbol{\sigma}^{n+1}} + \Delta\gamma_2 \frac{\boldsymbol{S}_2 \otimes \boldsymbol{S}_2}{|\boldsymbol{S}_2 : \boldsymbol{\sigma}^{n+1}|} + \Delta\gamma_3 \frac{\boldsymbol{S}_3 \otimes \boldsymbol{S}_3}{|\boldsymbol{S}_3 : \boldsymbol{\sigma}^{n+1}|} , \tag{4.14}$$

$$\alpha^{n+1} = \alpha^n + k_n\Delta\gamma_1 + k_s\Delta\gamma_2 + k_s\Delta\gamma_3 . \tag{4.15}$$

For the stress like variables:

$$\boldsymbol{\sigma}^{n+1} = \boldsymbol{\sigma}^{n+1}_{\text{trial}} - \mathbb{C}^n : \left[\Delta\gamma_1 \boldsymbol{S}_1 + \text{sign}(\boldsymbol{S}_2 : \boldsymbol{\sigma}^{n+1})\Delta\gamma_2 \boldsymbol{S}_2 + \text{sign}(\boldsymbol{S}_3 : \boldsymbol{\sigma}^{n+1})\Delta\gamma_3 \boldsymbol{S}_3\right] \tag{4.16}$$

and

$$q^{n+1} = f_n(1 - \exp[-H\alpha^{n+1}]) . \tag{4.17}$$

The algorithm given in Section 3 is used to advance the solution from time t^n to time t^{n+1}. The main issue to be addressed in using the algorithm is Step 4; i.e. how does one solve for the unknowns? Because Remark **3.2** applies to the proposed model, the problem reduces to a nonlinear root-finding problem in several variables. So as to make this root finding problem transparent, we first consider the case where only the tensile surface is active. The case of three active surfaces is considered after that and the case of two active surfaces is given by a trivial modification of the three-surface case.

When only the tensile surface is active, the problem to be solved is

$$\phi_1 = \boldsymbol{S}_1 : \boldsymbol{\sigma}^{n+1} - f_n + k_n q^{n+1} = 0 . \tag{4.18}$$

Substituting (4.16) and (4.17) into (4.18) gives a single nonlinear equation with only one unknown, $\Delta\gamma_1$:

$$\phi_1(\Delta\gamma_1) = \boldsymbol{S}_1 : \boldsymbol{\sigma}^{n+1}_{\text{trial}} - \Delta\gamma_1 \boldsymbol{S}_1 : \mathbb{C}^n : \boldsymbol{S}_1 - f_n + k_n f_n - k_n f_n \exp(-Hk_n\Delta\gamma_1) = 0 . \tag{4.19}$$

This equation can be solved using Newton's method or any other suitable root finder.

Remark 4.2.

Unlike conventional metal plasticity Equation (4.19) is not convex in $\Delta\gamma_1$; rather, it is concave. This follows by considering the second derivative of ϕ_1 with respect to $\Delta\gamma_1$:

$$\frac{\partial^2 \phi_1}{\partial \Delta\gamma_1{}^2} = -f_n k_n^2 H \exp(-H k_n \Delta\gamma_1) < 0\,. \tag{4.20}$$

Thus a qualitative plot of ϕ_1 reveals that the starting iterate for a Newton-like method must lie to the right of the curve's apex; see Figure 4. The apex location is given by the condition that $\frac{\partial \phi_1}{\partial \Delta\gamma_1} = 0$. A more simple way of choosing a starting value is to choose a value to the right of the desired root by setting $\exp(-H k_n \Delta\gamma_1)$ to zero in (4.19). This gives a starting value of

$$\Delta\gamma_1{}^0 = \frac{\boldsymbol{S}_1 : \boldsymbol{\sigma}_{\text{trial}}^{n+1} - (1 - k_n) f_n}{\boldsymbol{S}_1 : \mathbb{C}^n : \boldsymbol{S}_1}\,. \tag{4.21}$$

Algorithmically, this is a convenient formula because all the required quantities are also used elsewhere in the algorithm. □

Remark 4.3.

Once $\Delta\gamma_1$ has been solved for, Equations (4.14)-(4.17) may be used to update all the other required quantities. □

Remark 4.4.

If the single surface chosen had been ϕ_2, then the equation to be solved would have been

$$\begin{aligned} \phi_2(\Delta\gamma_2) = {} & |\boldsymbol{S}_2 : \boldsymbol{\sigma}_{\text{trial}}^{n+1} - \operatorname{sign}(\boldsymbol{S}_2 : \boldsymbol{\sigma}^{n+1}) \Delta\gamma_2 \boldsymbol{S}_2 : \mathbb{C}^n : \boldsymbol{S}_2| \\ & - f_s + k_s f_n - k_s f_n \exp(-H k_s \Delta\gamma_2) = 0\,. \end{aligned} \tag{4.22}$$

Note that $\operatorname{sign}(\boldsymbol{S}_2 : \boldsymbol{\sigma}^{n+1}) = \operatorname{sign}(\boldsymbol{S}_2 : \boldsymbol{\sigma}_{\text{trial}}^{n+1})$. This follows from Equation (4.16) when it is noted that $\Delta\gamma_2 \geq 0$ by the Kuhn-Tucker conditions and that $\boldsymbol{S}_2 : \mathbb{C}^n : \boldsymbol{S}_2 > 0$ for the material to satisfy the Second Law of Thermodynamics. Thus, the initial starting value for a Newton iteration method can be obtained in the same manner as above. This leads to:

$$\Delta\gamma_2{}^0 = \frac{|\boldsymbol{S}_2 : \boldsymbol{\sigma}_{\text{trial}}^{n+1}| - f_s + k_s f_n}{\boldsymbol{S}_2 : \mathbb{C}^n : \boldsymbol{S}_2}\,. \tag{4.23}$$

A similar result holds for ϕ_3. □

The case where all three surfaces are active requires the solution of a set of three nonlinear equations in three unknowns:

$$\begin{aligned} \phi_1(\Delta\gamma_k) &= \boldsymbol{S}_1 : \boldsymbol{\sigma}_{\text{trial}}^{n+1} - \Delta\gamma_1 \boldsymbol{S}_1 : \mathbb{C}^n : \boldsymbol{S}_1 - f_n + k_n q^{n+1}(\Delta\gamma_k) = 0 \\ \phi_2(\Delta\gamma_k) &= |\boldsymbol{S}_2 : \boldsymbol{\sigma}_{\text{trial}}^{n+1}| - \Delta\gamma_2 \boldsymbol{S}_2 : \mathbb{C}^n : \boldsymbol{S}_2 - f_s + k_s q^{n+1}(\Delta\gamma_k) = 0 \\ \phi_3(\Delta\gamma_k) &= |\boldsymbol{S}_3 : \boldsymbol{\sigma}_{\text{trial}}^{n+1}| - \Delta\gamma_3 \boldsymbol{S}_3 : \mathbb{C}^n : \boldsymbol{S}_3 - f_s + k_s q^{n+1}(\Delta\gamma_k) = 0\,. \end{aligned} \tag{4.24}$$

This set of equations can be solved, as in the single surface case, by using Newton's method. When doing so, the update formula for the vector of unknowns is given by

$$\Delta\gamma_k^{(i+1)} = \Delta\gamma_k^{(i)} + \delta[\Delta\gamma_k^{(i)}], \tag{4.25}$$

where the the superscripts in parentheses indicate Newton iteration numbers and

$$\delta[\Delta\gamma_k^{(i)}] = -\sum_{j=1}^{3} \bar{g}_{kj}^{-1(i)} \bar{d}_j^{(i)}. \tag{4.26}$$

In the above, the vector

$$\bar{\boldsymbol{d}}^{(i)} = \left\{ \begin{array}{c} \phi_1 \\ \phi_2 \\ \phi_3 \end{array} \right\}^{(i)} \tag{4.27}$$

and the matrix

$$\bar{\boldsymbol{g}}^{(i)} = \left[\begin{array}{ccc} \boldsymbol{S}_1 : \mathbb{C}^n : \boldsymbol{S}_1 - k_n \partial_{\Delta\gamma_1} q^{n+1} & -k_n \partial_{\Delta\gamma_2} q^{n+1} & -k_n \partial_{\Delta\gamma_3} q^{n+1} \\ & \boldsymbol{S}_2 : \mathbb{C}^n : \boldsymbol{S}_2 - k_s \partial_{\Delta\gamma_2} q^{n+1} & -k_s \partial_{\Delta\gamma_3} q^{n+1} \\ \text{sym.} & & \boldsymbol{S}_3 : \mathbb{C}^n : \boldsymbol{S}_3 - k_s \partial_{\Delta\gamma_3} q^{n+1} \end{array} \right]^{(i)}, \tag{4.28}$$

where

$$\begin{aligned} \partial_{\Delta\gamma_1} q^{n+1} &= f_n H k_n \exp(-H\alpha^{n+1}) \\ \partial_{\Delta\gamma_2} q^{n+1} &= \partial_{\Delta\gamma_3} q^{n+1} = f_n H k_s \exp(-H\alpha^{n+1}). \end{aligned} \tag{4.29}$$

Remark 4.5.

The initial guess for the iteration scheme can be chosen by applying the same technique as was used in the single surface case; i.e. by setting $\exp(-H\alpha^{n+1}) = 0$ and solving for $(\Delta\gamma_1{}^0, \Delta\gamma_2{}^0, \Delta\gamma_3{}^0)$. Note this produces the same starting value formulae as before, because the procedure of setting the exponential to zero uncouples the three equations. □

Remark 4.6.

To use the expressions given above, a knowledge of the material stiffness is required. As was mentioned before, the Sherwin-Morrison-Woodbury formula may be used to invert the compliance expression to give the stiffness. Doing so gives

$$\mathbb{C}^{n+1} = \mathbb{C}^n + \sum_{k=1}^{3} r_k (\mathbb{C}^n : \boldsymbol{S}_k) \otimes (\mathbb{C}^n : \boldsymbol{S}_k), \tag{4.30}$$

where

$$\begin{aligned} r_1 &= \frac{-\Delta\gamma_1}{\boldsymbol{S}_1 : \boldsymbol{\sigma}^{n+1} + \Delta\gamma_1 \boldsymbol{S}_1 : \mathbb{C}^n : \boldsymbol{S}_1} \\ r_2 &= \frac{-\Delta\gamma_2}{|\boldsymbol{S}_2 : \boldsymbol{\sigma}^{n+1}| + \Delta\gamma_2 \boldsymbol{S}_2 : \mathbb{C}^n : \boldsymbol{S}_2} \\ r_3 &= \frac{-\Delta\gamma_3}{|\boldsymbol{S}_3 : \boldsymbol{\sigma}^{n+1}| + \Delta\gamma_3 \boldsymbol{S}_3 : \mathbb{C}^n : \boldsymbol{S}_3}. \end{aligned} \tag{4.31}$$

□

Remark 4.7.

Crack closure is easily incorporated into this scheme by setting the material stiffness to its undamaged value whenever $\boldsymbol{S}_1 : \boldsymbol{\sigma} < 0$. Upon re-encountering a state where $\boldsymbol{S}_1 : \boldsymbol{\sigma} \geq 0$ the damaged stiffness tensor can be "recovered". □

4.5. Algorithmic Tangents.

When solving initial boundary value problems it is often desirable to have the algorithmic tangent modulus of the material model. Note that this modulus differs from the continuum tangent modulus as was pointed out by SIMO & TAYLOR [1986]. By following the well established procedure presented in SIMO [1993], the tangent modulus for the case of only the tensile surface active is given by

$$\mathbb{C}^{n+1}_{\text{algo}} = \mathbb{C}^n - \frac{(\boldsymbol{S}_1 : \mathbb{C}^n) \otimes (\boldsymbol{S}_1 : \mathbb{C}^n)}{\boldsymbol{S}_1 : \mathbb{C}^n : \boldsymbol{S}_1 - k_n^2 f_n H \exp(-H\alpha^{n+1})} . \tag{4.32}$$

In the three surface case, the identical procedure leads to the following expression for the tangent modulus:

$$\mathbb{C}^{n+1}_{\text{algo}} = \mathbb{C}^n - \sum_{k=1}^{3} \sum_{j=1}^{3} \bar{g}^{-1}_{kj} (\partial_\sigma \phi_k) \otimes (\partial_\sigma \phi_j) , \tag{4.33}$$

where the matrix $\bar{\boldsymbol{g}}$ is given in (4.28). Note in particular that the algorithmic tangent is symmetric.

4.6. Rate Effects.

As was noted before, the rate dependent case can be trivially treated once the rate independent case has been worked out. In particular, the system of three equations that must be solved in the rate independent case (4.24) are trivially modified by replacing $\Delta\gamma_k$ by $\frac{<\phi_k^{n+1}>\Delta t}{\eta}$. This results in the following three equations that must be simultaneously solved for $\frac{<\phi_k^{n+1}>\Delta t}{\eta}$:

$$\begin{aligned}
&\boldsymbol{S}_1 : \boldsymbol{\sigma}^{n+1}_{\text{trial}} - (\boldsymbol{S}_1 : \mathbb{C}^n : \boldsymbol{S}_1 + \frac{\eta}{\Delta t}) \frac{<\phi_1^{n+1}>\Delta t}{\eta} - f_n + k_n q^{n+1} (\frac{<\phi_k^{n+1}>\Delta t}{\eta}) = 0 \\
&|\boldsymbol{S}_2 : \boldsymbol{\sigma}^{n+1}_{\text{trial}}| - (\boldsymbol{S}_2 : \mathbb{C}^n : \boldsymbol{S}_2 + \frac{\eta}{\Delta t}) \frac{<\phi_2^{n+1}>\Delta t}{\eta} - f_s + k_s q^{n+1} (\frac{<\phi_k^{n+1}>\Delta t}{\eta}) = 0 \\
&|\boldsymbol{S}_3 : \boldsymbol{\sigma}^{n+1}_{\text{trial}}| - (\boldsymbol{S}_3 : \mathbb{C}^n : \boldsymbol{S}_3 + \frac{\eta}{\Delta t}) \frac{<\phi_3^{n+1}>\Delta t}{\eta} - f_s + k_s q^{n+1} (\frac{<\phi_k^{n+1}>\Delta t}{\eta}) = 0 .
\end{aligned} \tag{4.34}$$

The iteration method (4.25)-(4.28) can still be employed to solve these equations through a couple of trivial modifications. One, replace instances of $\boldsymbol{S}_k : \mathbb{C}^n : \boldsymbol{S}_k$ by $\boldsymbol{S}_k : \mathbb{C}^n : \boldsymbol{S}_k + \frac{\eta}{\Delta t}$ in $\bar{\boldsymbol{g}}$ and, two, replace $\bar{\boldsymbol{d}}$ by the residual of (4.34). The starting values for the iteration scheme are obtained from the rate independent formulas by replacing $\Delta\gamma_k^0$ by $\left(\frac{<\phi_k^{n+1}>\Delta t}{\eta}\right)^0$ on the left hand side and $\boldsymbol{S}_k : \mathbb{C}^n : \boldsymbol{S}_k$ by $\boldsymbol{S}_k : \mathbb{C}^n : \boldsymbol{S}_k + \frac{\eta}{\Delta t}$ on the right hand side. The identical substitutions also convert the rate independent algorithmic moduli (4.32) and (4.33) to the rate dependent case.

Remark 4.8.

The regularizing effect of viscosity (NEEDLEMAN [1987]) is now transparently seen through its effect on the algorithmic tangent moduli. Consider the single surface case given in Equation (4.32) which converts to

$$\mathbb{C}^{n+1}_{\text{algo,visc}} = \mathbb{C}^n - \frac{(\boldsymbol{S}_1 : \mathbb{C}^n) \otimes (\boldsymbol{S}_1 : \mathbb{C}^n)}{(\boldsymbol{S}_1 : \mathbb{C}^n : \boldsymbol{S}_1 + \frac{\eta}{\Delta t}) - k_n^2 f_n H \exp(-H\alpha^{n+1})} . \tag{4.35}$$

Stability of a Newton-Raphson finite element global solver will depend strongly on how close the denominator of the second term on the right is to zero. The effect of the viscosity is easily seen to make the denominator more positive and to lessen any numerical ill-conditioning caused by a small denominator. Note however that one may be required to decrease the time step Δt appreciably to take advantage of this effect — depending, of course, on the material properties. Thus viscous behavior is seen to provide an added stabilizing effect on numerical calculations for sufficiently small time steps — in addition to providing an implicit characteristic length scale for the model. □

4.7. Example Calculations.

To close this section, a series of numerical examples are provided to demonstrate the effectiveness of the model. The first example is concerned with plain concrete and examines the effect of the shear surfaces ϕ_2 and ϕ_3. The second example is the analysis of a notched plain concrete beam in three point bending. The third example is the analysis of a lightly reinforced beam under three point bending and the last example is the analysis of an overly reinforced beam under three point bending.

Calculations were made using either the finite element code FEAP from the University of California at Berkeley or the finite element code NIKE3D from the Lawrence Livermore National Laboratory. All calculations were done with 8 noded brick elements with a standard Galerkin formulation and the characteristic length method described above.

Tapered Wedge

In this example a tapered wedge is analyzed. The geometry, material properties, and loading for this example are shown in Figure 5; the loading is displacement controlled across the entire top face of the wedge. The three hidden faces in Figure 5 are symmetry planes. Shown in Figure 6 are two load–deflection plots for the response of the wedge on its top face. The dashed line represents the analysis when only surface ϕ_1 (no shear surfaces considered) is used in the calculation and the solid line represents the analysis when all three damage surfaces are employed. The two curves remain identical up to a displacement of 0.0013 inches where they diverge with the solid line giving a more realistic result. This is due to the 3-D nature of the stress field near the centerline of the wedge where the smeared crack normals are not perfectly parallel to the horizontal plane. The result is that the imposed loading produces shear stresses across these crack planes. In the case of the solid line, the damage surfaces ϕ_2 and ϕ_3 become activated and control and degrade this transmission of stress – resulting in the total separation of the block. In the

case of the dashed line, these shear stresses are not controlled and eventually become the dominant mechanism for the transfer of load across the smeared crack planes – resulting, eventually, in the load–displacement plot having a non-physical positive slope at large extensions. The control shear stresses (tractions) across smeared crack planes is clearly required for problems of this nature.

Notched Plain Concrete Beam

In this example a notched plain concrete beam in 3 point bending is analyzed. The geometry, material properties, and loading for this example are shown in Figure 7, where the rear face and left end of the geometry shown are symmetry planes. The material properties given are the mean values reported from experiments conducted at the Naval Civil Engineering Laboratory on this beam geometry; see MALVAR & WARREN [1988] and MALVAR & FOURNEY [1990]. The critical shear value was obtained from a simple Mohr's circle argument as half of the reported compressive strength, $f_c' = 4206$ psi; the tensile retention value was chosen for numerical stability close to machine zero and the shear retention value was arbitrarily set to a moderately small number. In the range chosen the actual value of the shear retention parameter does not affect the beam's overall response appreciably. The calculation itself was displacement controlled. As the deflection is increased, the calculation results predict a narrow smeared crack originating at the notch root and propagating up the center of the span. The resulting load–deflection curve under the load point is plotted in Figure 8; the solid line is the calculation and the triangles represent the mean of the data from several experimental runs. The overall agreement is seen to be reasonably good and adjustment of the mesh and the properties would likely improve the agreement. Note that agreement beyond a deflection of 0.018 in. deteriorates rapidly. This is due to the fact that the response of the beam is effectively governed by only a few 8 noded brick elements in the top fibers of the beam and these elements are known to respond poorly in pure bending.

Moderately Reinforced Concrete Beam

In this example, a moderately reinforced beam under 3 point displacement driven bending is analyzed. The geometry, material properties, and loading for this example are shown in Figure 9, where the left face and the rear face are symmetry planes. This problem corresponds to an experiment conducted by BURNS & SEISS [1962] — beam J4. Note, however, that for simplicity the reinforcing pattern for this beam was altered by removing the stirrups in the same fashion as in KWAK & FILIPPOU [1990]. The material properties are those reported by BURNS & SEISS [1962] where indicated. The tensile shear strength of the concrete was estimate using the relation $f_n = 5\sqrt{f_c'}$ where f_c' was reported to be 4820 psi; the shear strength was estimated to be 5 times the tensile strength. The Young's modulus of the concrete was taken from KWAK & FILIPPOU [1990]. The remaining concrete properties were arbitrarily set within the spread of data for concrete. For the rebar, the hardening modulus was estimated from the experimental data.

In the calculation, as the loading is applied to the beam, a diffuse crack field propagates up from the lower fibers of the beam with a dominant crack in the center of the span. The cracks furthest from the centerline of the beam also curve in towards the loading. This

description corresponds well to the observed crack pattern. Figure **10** shows the resulting load–deflection curve underneath the load point; the solid line is the calculation and the triangles are the data. Up to a load of about 10 kips the beam behaves elastically. At this point the concrete starts to crack and load is transferred into the reinforcing rods (which were discretely modeled with elasto-plastic beam elements). When the reinforcing rods reach their yield point the beam loses almost all of its tangent stiffness, as indicated by both the data and the calculation results in the figure. Note that in this calculation the effects of the shear damage surfaces are not appreciable until the reinforcing rods begin to yield and, that after yielding, the slope of the load–deflection curve is strongly governed by both the hardening modulus of the reinforcing rods and the shear degradation properties of the concrete. As noted in the original report and later by KWAK AND FILIPPOU [1990], for the level of loading shown, the effect of reinforcing rod slippage is minimal.

Heavily Reinforced Concrete Beam

In this example, an overly reinforced beam (1.53% volume of rebar) under 3 point bending is analyzed. The geometry, material properties, and loading for this example are shown in Figure **11**, where the left face and the rear face are symmetry planes; (the stirrup spacing is 8.25 inches). The beam corresponds to an experiment reported in BRESLER & SCORDELIS [1963] — beam A1. The tensile strength of the concrete was estimated to be roughly one-tenth of the reported compressive strength of 3.49 ksi and the shear strength of the concrete was estimated to be roughly half of this value. The Young's modulus and Poisson ratio were taken from KWAK & FILIPPOU [1990] and the remaining concrete properties were estimated within the acceptable range for concrete. The hardening moduli for the reinforcing rods were estimated from the given data — note however that there is no rebar yield in this calculation.

The heavy reinforcing pattern makes the inclusion of bar slip in this example important. For the calculation, the bar slip behavior was modeled with a simplistic stick–slip law which was implemented in the 1-D slideline logic in NIKE3D by MAKER & LAURSEN [1993]. A slip value of 150 psi for a wetted area load was chosen by trial and error.

In the calculation (displacement controlled), load results in a very diffuse crack field which propagates from the lower fibers of the beam towards the top. This crack field eventually forms a series of prominent cracks spaced out along the length of the beam and the overall crack field tends to point towards the load point. Figure **13** shows the smeared crack field projected onto the outer face of the beam half way through the loading; the intensity of the crack opening is indicated by the intensity of the shading. Note, in particular, that horizontal cracks underneath the load point are predicted by the model. The overall crack field qualitatively corresponds well to the observed experiment. Figure **14** shows the resulting load–deflection curve underneath the load point; the solid line represents the calculation and the triangles represent the data. The agreement is seen to be good. If the slippage of the bar had not been included in the calculation, the predicted response of the beam would have diverged sharply from the actual data around a deflection of about 0.3 inches.

§5. Closure

An alternative framework for continuum damage mechanics has been exploited in the design and numerical implementation of a constitutive model for the tensile failure of plain concrete. For a given failure surface, often specified via experimental testing, the model automatically furnishes a generally fully anisotropic damage evolution law under the single assumption of maximum (damage) dissipation. Once the failure surface is specified, no adjustable parameters are present in the model. A detailed algorithmic treatment has been presented which addresses issues related to time integration as well as regularization approaches leading to mesh–independent calculations. Although no spurious mesh–dependencies arise, the global solution to the initial boundary value problem generally retains the characteristic lack of uniqueness inherent to this class of problems. In spite of recent advances, the design of robust procedures for dealing with this issue remains unsettled.

The proposed three failure surface model for plain concrete exhibits remarkably good agreement with experimental results, thus lending support to the hypothesis of maximum dissipation that dictates the form of the damage rule. It is emphasized that the proposed damage model for the brittle failure of concrete contains a minimal set of material constants, which can be determined from standard tests.

§ Acknowledgements

The authors would like to thank Dr. Goudreau of the Lawrence Livermore National Laboratory for sponsoring this work, Prof. Filippou of the University of California at Berkeley for many helpful discussions on the behavior of concrete, Drs. Maker and Whirley of the Lawrence Livermore National Laboratory for their help in implementing versions of the model in the LLNL finite element codes DYNA3D and NIKE3D, and Prof. Taylor of the University of California at Berkeley for many helpful discussions and for graciously providing a version of his finite element code FEAP for the development of the model.

§ References

BAŽANT, Z.P. & BELYTSCHKO, T. [1985], "Wave Propagation in a Strain Softening Bar; Exact Solution," *J. Eng. Mech.*, **111** 381-389.

BAŽANT, Z.P. & OH, B.H. [1983], "Crack band theory for fracture of concrete," *Mater. Constr.*, **16**(93), 155-177.

BRESLER, B. & SCORDELIS, A.C. [1963], "Shear Strength of Reinforced Concrete Beams," *J. Amer. Conc. Inst.*, **60**, 51-72.

BRUNS, N.H. & SEISS, C.P. [1962], "Load–Deformation Characteristics of Beam–Column Connections in Reinforced Concrete," *Civil Engineering Studies,* **SRS No. 234**.

DEBORST, R. [1991], "Simulation of Strain Localization: A Reappraisal of the Cosserat Continuum," *Eng. Comp.*, **8**, 317-332.

DEBORST, R. [1987], "Computation of Post-Bifurcation and Post-Failure Behavior of Strain-Softening Solids," *Comp. Struc.*, **25**, 211-224.

DEBORST, R. & NAUTA, P. [1985], "Non-Orthogonal Cracks in a Smeared Finite Element Model," *Eng. Comp.*, **2**, 35-46.

DENNIS, J.E. JR. & SCHNABEL, R.B. [1983], "Numerical Methods for Unconstrained Optimization and Nonlinear Equations," Prentice-Hall.

GOVINDJEE, S. & SIMO, J.C. [1992], "Transition from Micro-Mechanics to Computationally Efficient Phenomenology: Carbon Black Filled Rubbers Incorporating Mullins' Effect," *J. Mech. Phys. Solids*, **40**, 213-233.

HILL, R. [1983], "The Mathematical Theory of Plasticity," Oxford University Press.

KACHANOV, L.M. [1958], "On Creep Rupture Time," *IZV Akad. Nauk SSSR*, Otd. Techn. Nauk, **8**, 26-31.

KOITER, W.T. [1953] "Stress-strain relations, uniqueness and variational theorems for elastic-plastic materials with a singular yield surface," *Quart. Appl. Math.*, **11**, 350-354.

KWAK, H.G. & FILIPPOU, F.C. [1990] "Finite Element Analysis of Reinforced Concrete Structures Under Monotonic Loads," *Report No. UCB/SEMM-90/14*, University of California at Berkeley, Department of Civil Engineering.

LEMAITRE, J.L. [1992], "A Course on Damage Mechanics," Springer-Verlag.

LUENBERGER, D.G. [1984], "Linear and Nonlinear Programming," Addison-Wesley.

MAKER, B.N. & LAURSEN, T.A. [1993], "A Finite Element Formulation for Rod/Continua Interactions: The One Dimensional Slideline," *Int. J. Num. Meth. Eng.*, to appear.

MALVAR, L.J. & FORNEY, M.E. [1990], "A Three Dimensional Application of the Smeared Crack Approach," *J. Eng. Frac. Mechanics,* **35**, 251-260.

MALVAR, L.J. & WARREN, G.E. [1988], "Fracture Energy of Three-Point-Bend Tests on Single-Edge-Notched Beams," *Exper. Mechanics,* 251-260.

NEEDLEMAN, A. [1987], "Material Rate Dependence and Mesh Sensitivity in Localization Problems," *Comp. Meth. Appl. Mech. Eng.,* **67**, 68-85.

OLIVER, J. [1989], "A Consistent Characteristic Length of Smeared Cracking Models," *Int. J. Num. Meth. Eng.,* **28**, 461-474.

ORTIZ, M. [1985], "A Constitutive Theory for the Inelastic Behavior of Concrete," *Mechanics of Materials,* **4**, 67-93.

PIETRUSZCZAK, ST. & MRÓZ, Z. [1981], "Finite Element Analysis of Deformation of Strain-Softening Materials," *Int. J. Num. Meth. Eng.,* **17**, 327-334.

PIJAUDIER-CABOT, G. & BAŽANT, Z.P. [1987], "Nonlocal Damage Theory," *J. Eng. Mech.,* **113**, 1512-1533.

RASHID, Y.R., [1968], "Ultimate Strength Analysis of Prestressed Concrete Pressure Vessels," *Nuclear Eng. Design,* **7**, 334-344.

READ, H.E. & HEGEMIER, G.A. [1984], "Strain Softening of Rock, Soil and Concrete – A Review Article," *Mechanics of Materials,* **3**, 271-294.

SIMO, J.C. [1988a], "Some Aspects of Continuum Damage Mechanics and Strain Softening," Contract report to Aptek Inc. for contract No. DNA-001-85-C-0264.

SIMO, J.C. [1988b], "Strain Softening and Dissipation: A Unification of Approaches," In: Cracking and Damage, Edited by Bažant, Z.P. and Mazars, J., 440-461.

SIMO, J.C. [1993], "Topics in the Numerical Analysis and Simulation of Classical Plasticity," in *Handbook for Numerical Analysis*, Volume III, P.G. Ciarlet and J.L. Lions Editors, North-Holland (in press).

SIMO, J. C., & JU, J.W., [1987], "Strain- and Stress-Based Continuum Damage Models–I. Formulation," *Int. J. Solids Struct.*, **23**, 821-840.

SIMO, J.C., KENNEDY, J.G., & GOVINDJEE, S. [1988], "Non-Smooth Multisurface Plasticity and Viscoplasticity. Loading/Unloading Conditions and Numerical Algorithms," *Int. J. Num. Meth. Eng.*, **26**, 2161-2185.

SIMO, J.C., OLIVER, J., AND ARMERO, F. [1993], "An Analysis of Strong Discontinuities Induced by Strain-Softening in Rate–Independent Inelastic Solids," *Comp. Mech.*, **12**, (in press).

SIMO, J.C. & TAYLOR, R.L. [1986], "Consistent Tangent Operators for Rate Independent Elastoplasticity," *Comp. Meth. Appl. Mech. Eng.*, **48**, 101-118.

SCHREYER, H.L. [1990], "Analytical Solutions for Nonlinear Strain-Gradient Softening and Localization," *J. Appl. Mech.*, **57**, 522-528.

SLUYS, L.J., [1992], "Wave Propagation, Localization and Dispersion in Softening Solids," Doctoral Thesis: Delft University of Technology.

TRUESDELL, C. & NOLL, W. [1965], "The Non-linear Field Theories of Mechanics," in *Handbuch der Physik,* Band III/3, Edited by: Flügge, S., Springer Verlag.

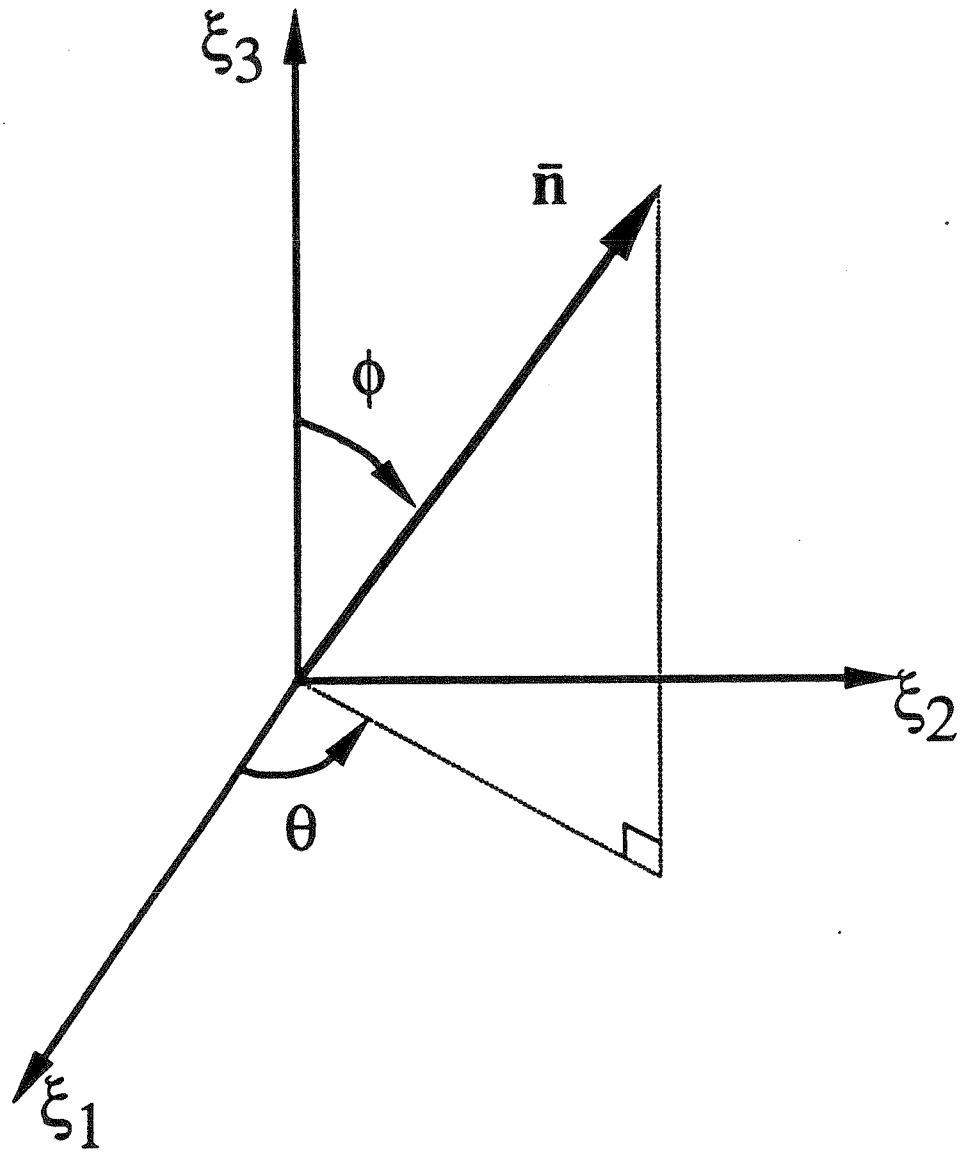

Figure 1. Smeared crack normal in the isoparametric space.

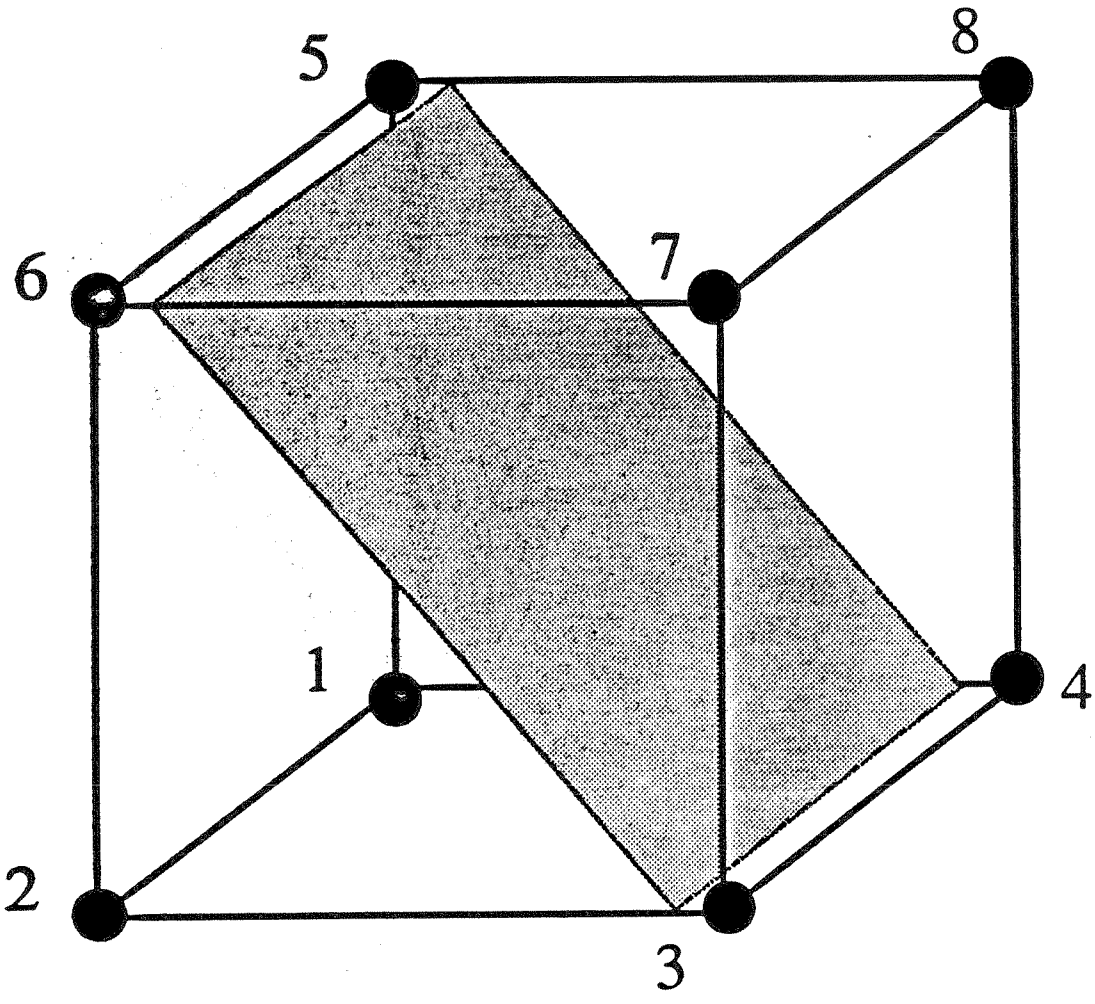

Figure 2. Standard node numbering scheme for 8 noded brick element and orientation of crack plane for Case 1.

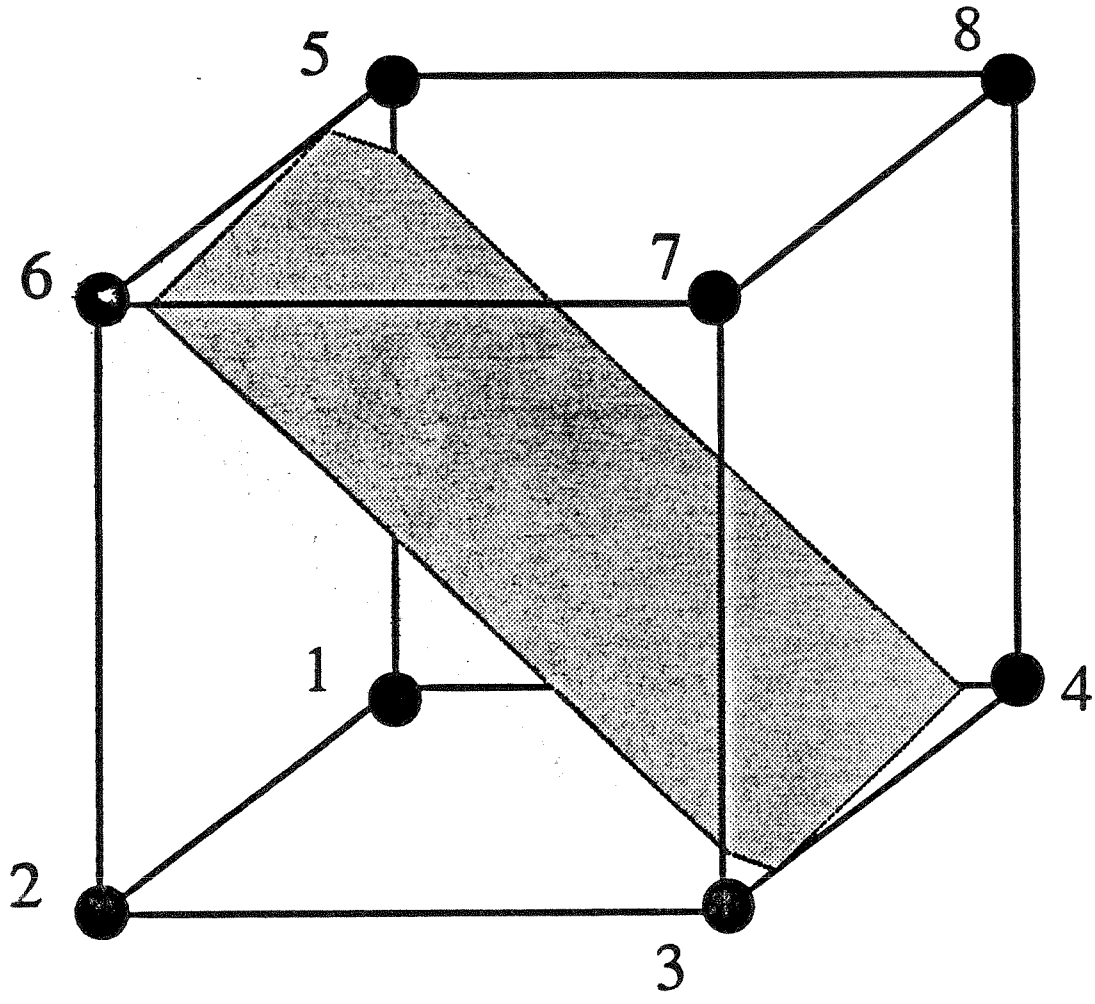

Figure 3. Orientation of crack plane for Case 2.

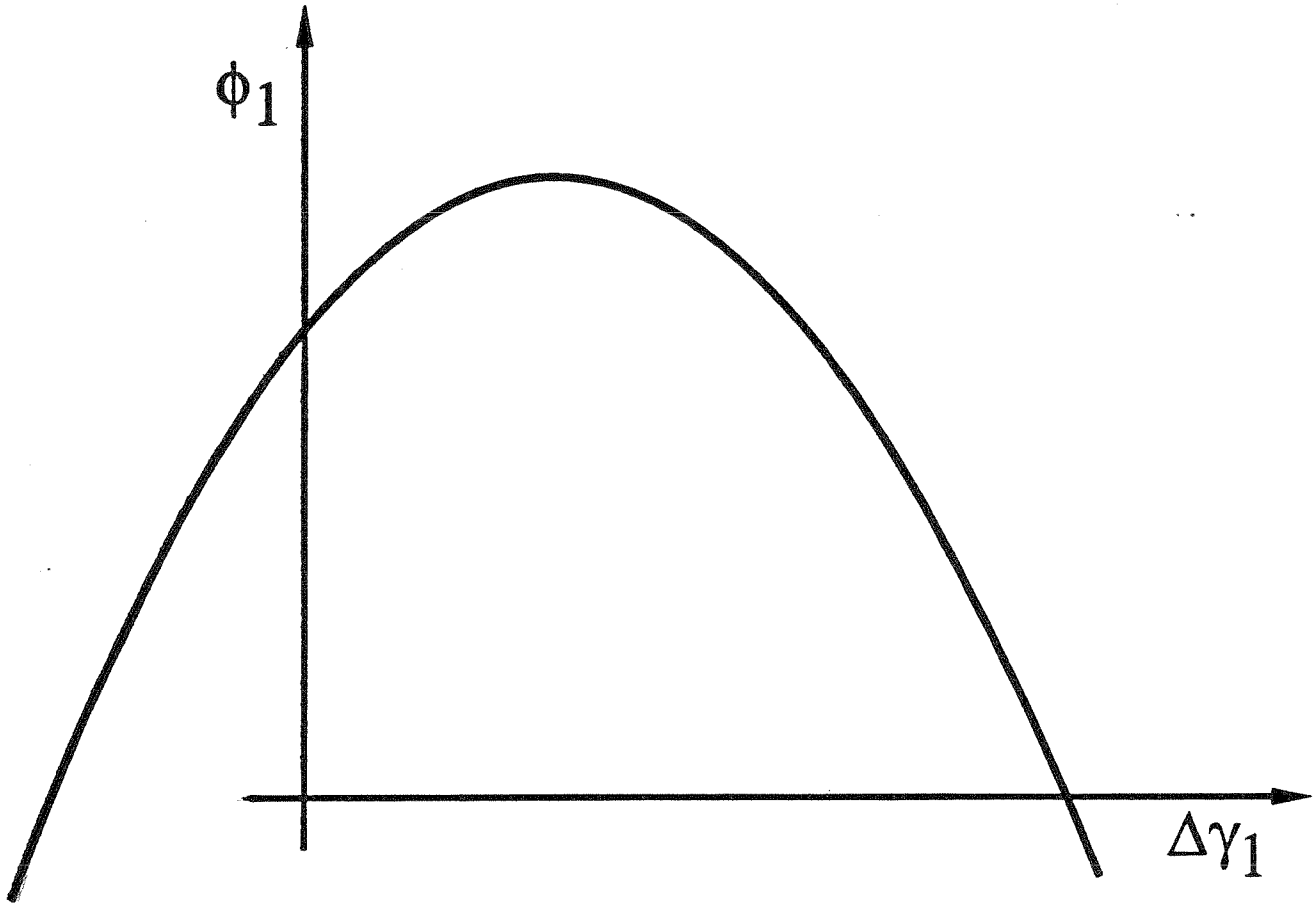

Figure 4. Concave character of damage surface as a function of the algorithmic consistency parameter.

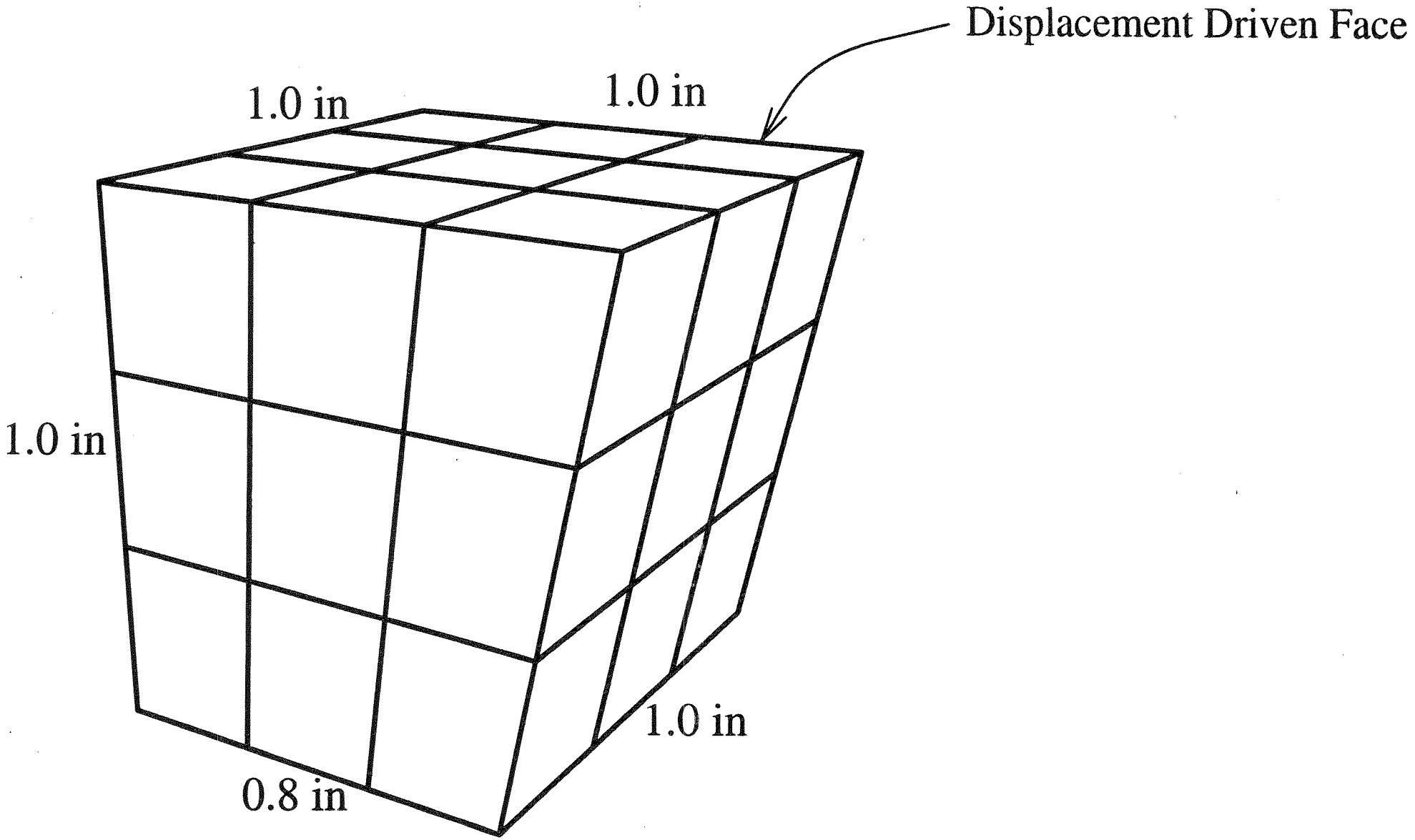

Figure 5. Tapered wedge shown in one-eighth symmetry with 27 8 noded brick elements. Material properties: $E = 4 \times 10^6$ psi, $\nu = 0.21$, $f_n = 400$ psi, $f_s = 2000$ psi, $\beta_s = 0.01$, $G_f = 1.72$ lbs/in, and $\eta = 0$ psi-sec.

Figure 6. Load versus displacement response for tapered wedge example. The solid line gives the response when both tensile and shear tractions are taken into account. The dashed line gives the response when only tensile tractions are accounted for.

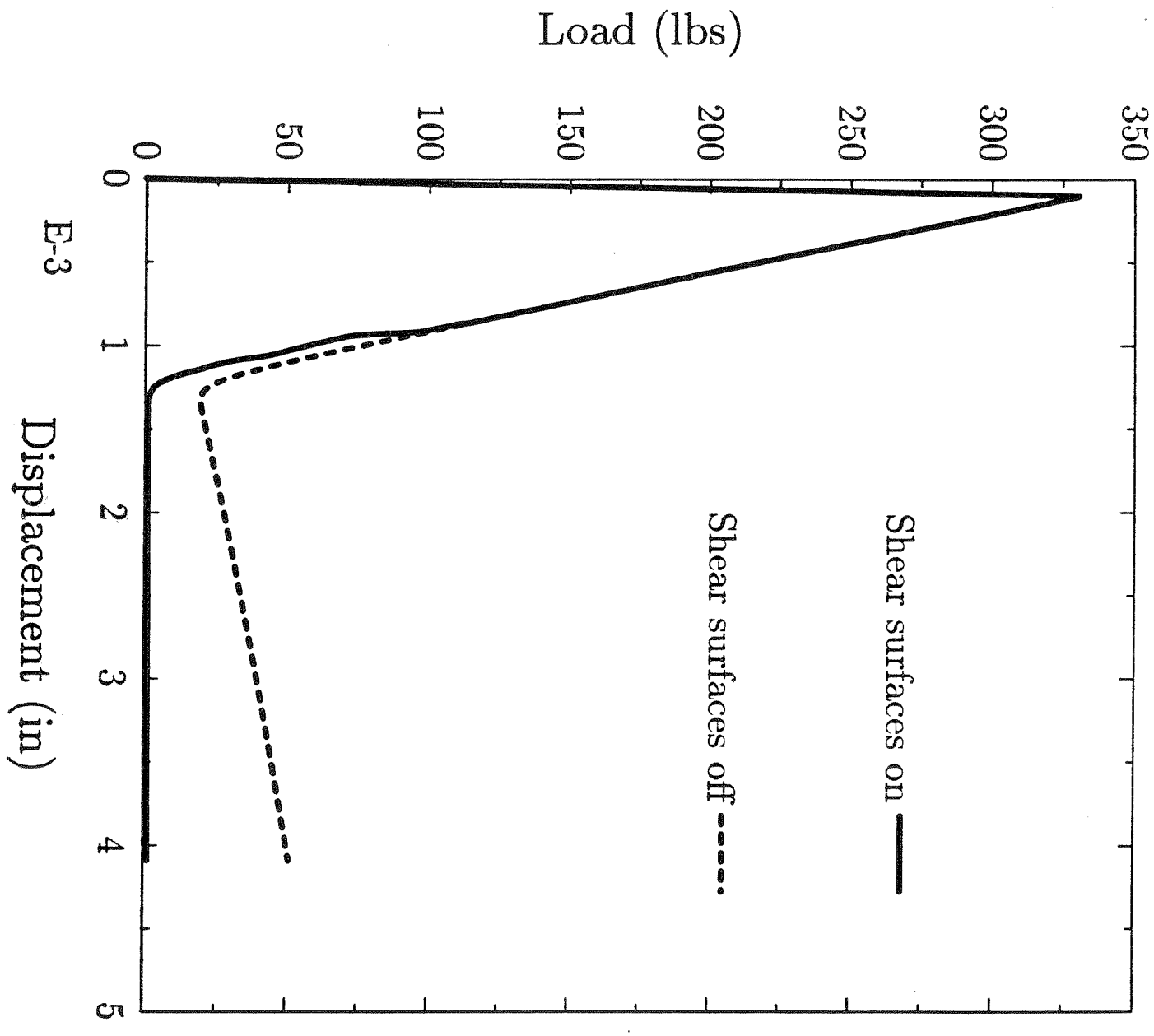

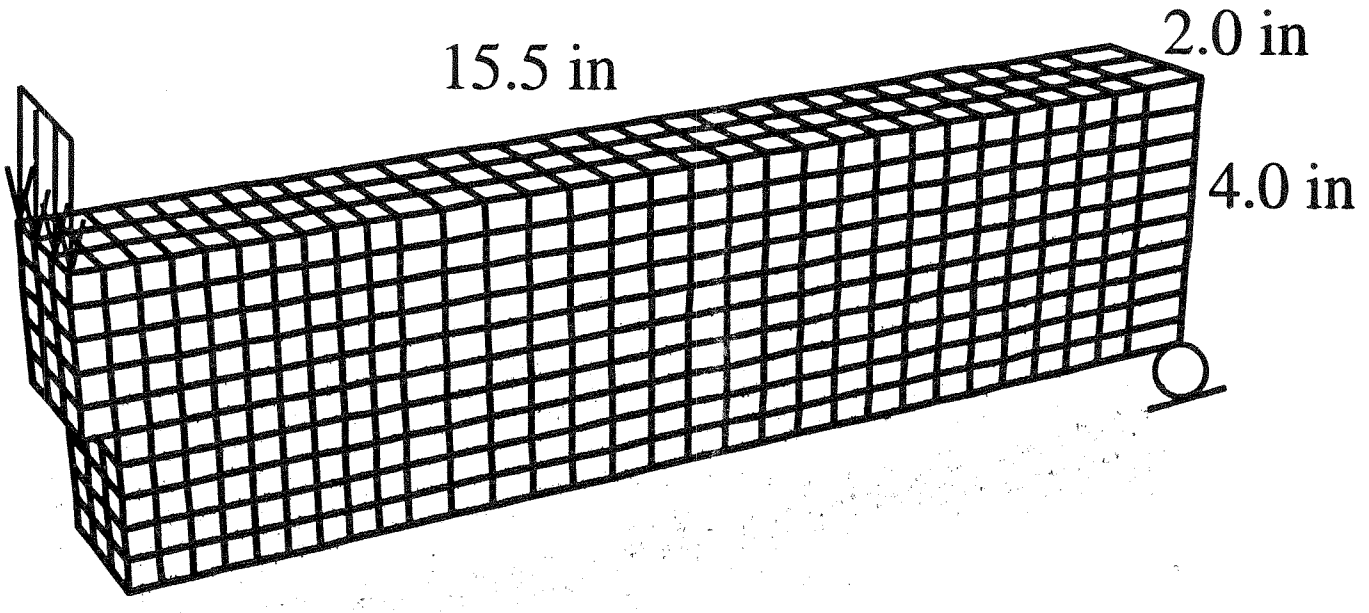

Figure 7. Finite element discritization of the notched plain concrete beam. The beam is shown in quarter symmetry. Material properties reported: $E = 3.15 \times 10^6$ psi, $f_n = 449.6$ psi, and $G_f = 0.436$ lbs/in. Material properties estimated: $\nu = 0.2$, $f_s = 2103$ psi, $\beta_s = 0.03$, $\eta = 0$ psi-sec.

Figure 8. Load versus displacement curves under the load point for the notched plain concrete beam. The solid line gives the calculation and the triangles give the experimental data MALVAR & FOURNEY [1990].

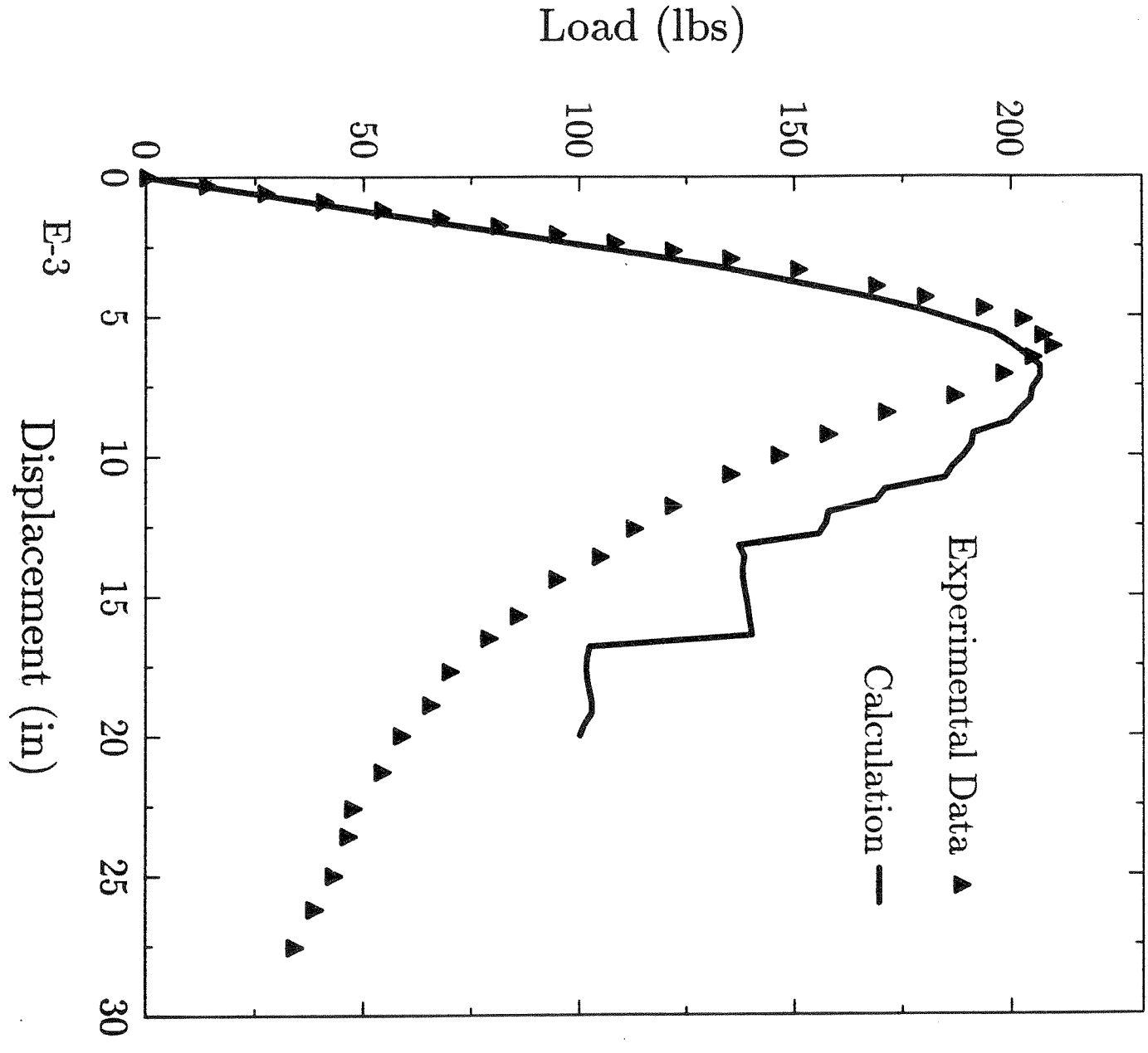

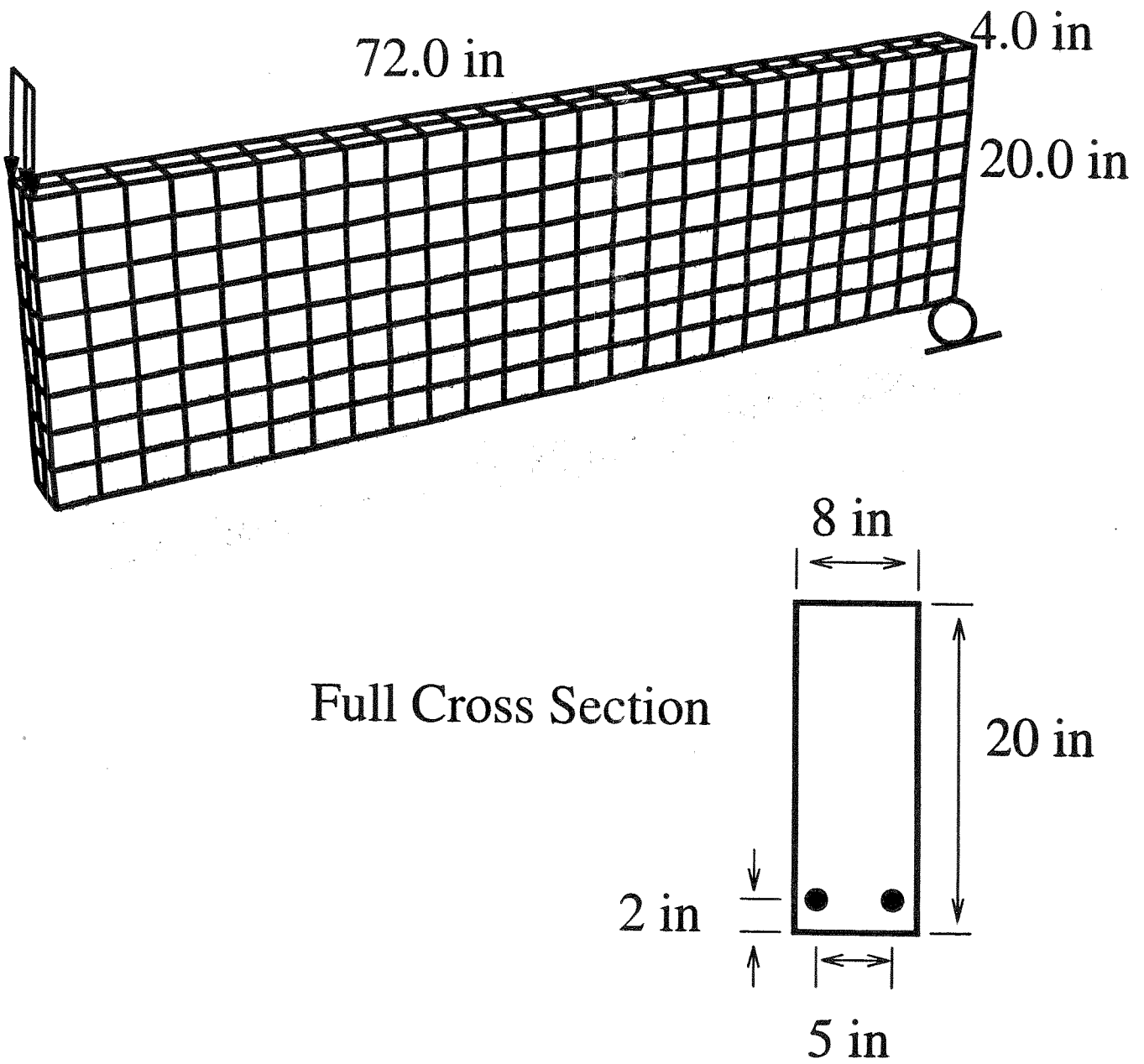

Figure 9. Finite element discritization of the moderately reinforced concrete beam. The beam is shown in quarter symmetry with the inset showing the reinforcing pattern. Material properties reported: (concrete) $E = 3.5 \times 10^6$ psi, (rebar) $E = 29.5 \times 10^6$ psi, and $\sigma_y = 44.9 \times 10^3$ psi. Material properties estimated: (concrete) $\nu = 0.2$, $f_n = 350$ psi, $f_s = 1750$ psi, $\beta_s = 0.05$, $G_f = 1.0$ lbs/in, $\eta = 0$ psi-sec, (rebar) $\nu = 0.3$, and $H = 27.0 \times 10^3$ psi.

Figure 10. Load versus displacement curves under the load point for the moderately reinforced concrete beam. The solid line gives the calculation and the triangles give the experimental data BURNS & SEISS [1962].

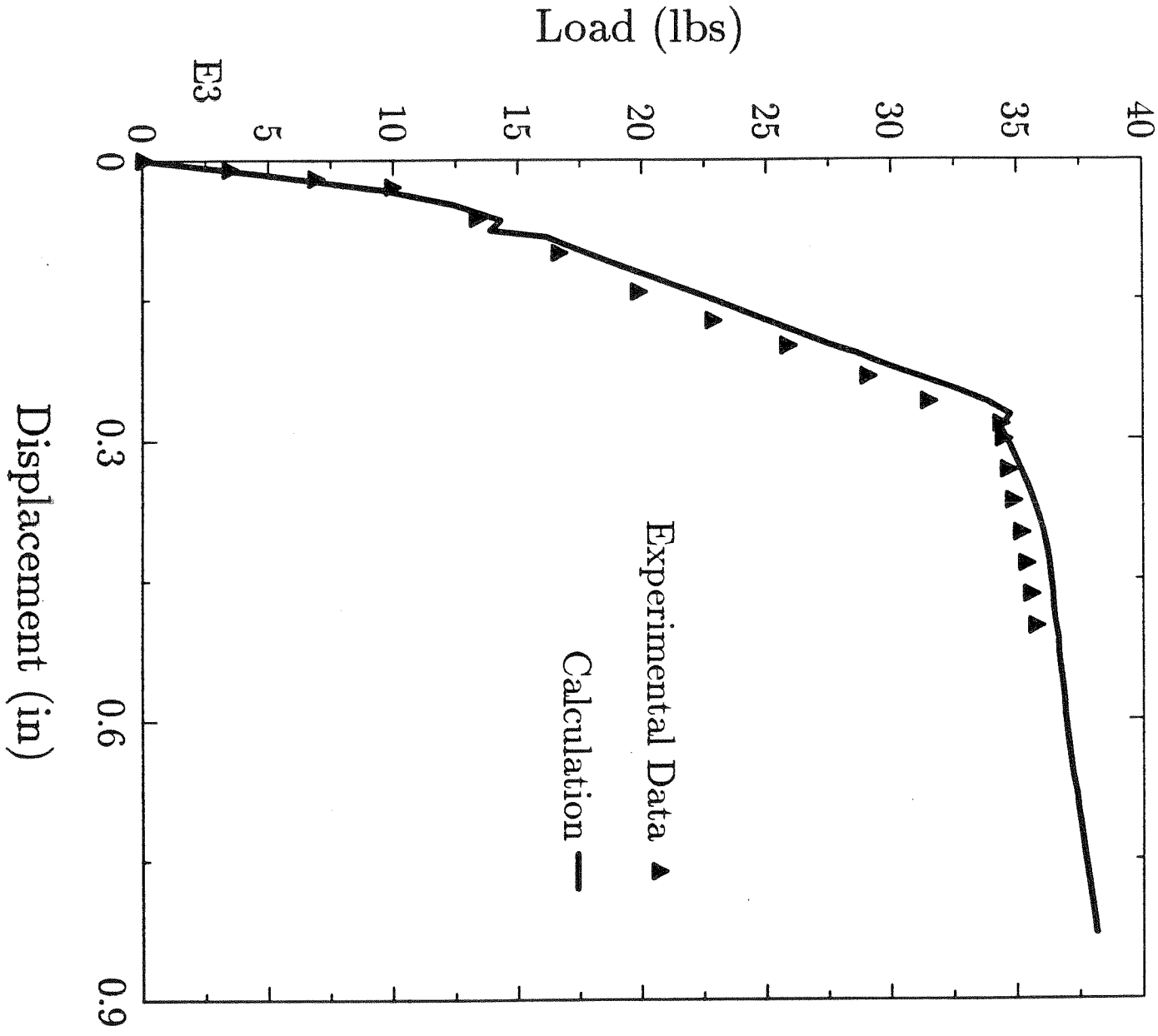

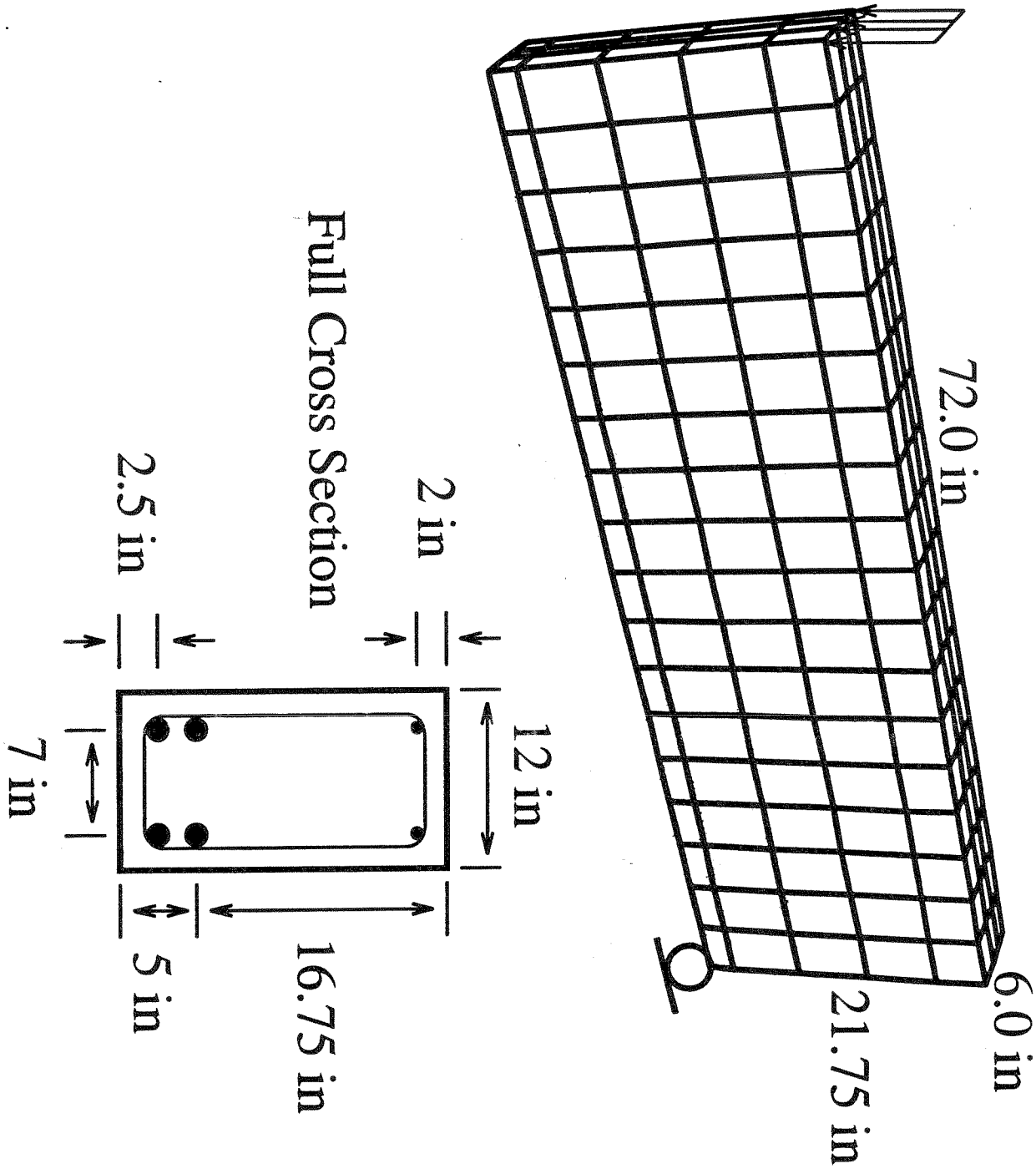

Figure 11. Finite element discritization of the heavily reinforced concrete beam. The beam is shown in quarter symmetry with the inset showing the reinforcing pattern. Material properties of concrete (all estimated): $E = 3.4 \times 10^6$ psi, $\nu = 0.167$, $f_n = 350$ psi, $f_s = 1750$ psi, $\beta_s = 0.05$, $G_f = 4.0$ lbs/in, and $\eta = 0$ psi-sec. Material properties of lower four rebar (#9's): (reported) $E = 31.6 \times 10^6$ psi, (estimated) $\nu = 0.3$, (reported) $\sigma_y = 80.5 \times 10^3$ psi, and (estimated) $H = 31.6 \times 10^3$ psi. Material properties of upper two rebar (#4's): (reported) $E = 29.2 \times 10^6$ psi, (estimated) $\nu = 0.3$, (reported) $\sigma_y = 50.1 \times 10^3$ psi, and (estimated) $H = 29.2 \times 10^3$ psi. Material properties of stirrups rebar (#2's): (reported) $E = 27.5 \times 10^6$ psi, (estimated) $\nu = 0.3$, (reported) $\sigma_y = 47.2 \times 10^3$ psi, and (estimated) $H = 27.5 \times 10^3$ psi. Material properties of upper two

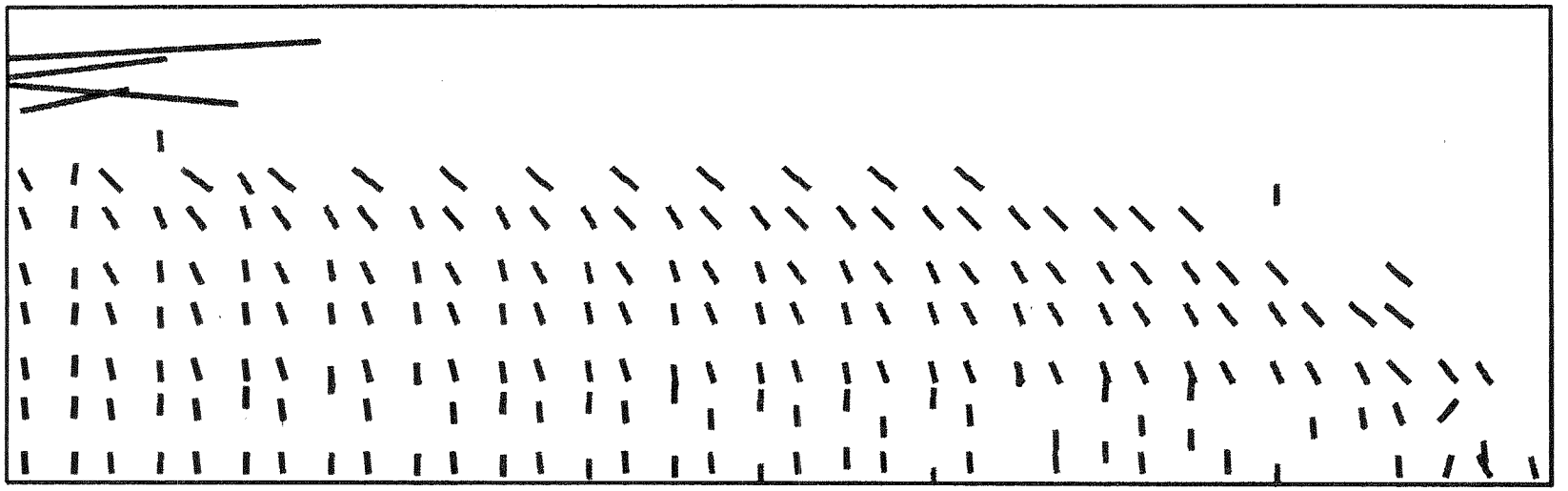

Figure 12. Smeared crack pattern projected onto the side of the beam shown in half symmetry. The intensity of the shading indicates the intensity of crack opening (damage).

Figure 13. Load versus displacement curves under the load point for the heavily reinforced concrete beam. The solid line gives the calculation and the triangles give the experimental data BRESLER & SCORDELIS [1963].